Report J-910900-4

Experimental Investigation of a High-Intens R-F Radiant Energy Source to Simulate th Thermal Environment in a Nuclear Light Bulb Engine

NASA Contract No. SNPC-70

UNITED AIRCRAFT CORPORATION

United Aircraft Research Laboratories

EAST HARTFORD, CONNECTICUT

United Aircraft Research Laboratories

UNITED AIRCRAFT CORPORATION

EAST HARTFORD, CONNECTICUT

Report J-910900-4

Experimental Investigation of a High-Intensity R-F Radiant Energy Source to Simulate the Thermal Environment in a Nuclear Light Bulb Engine

NASA Contract No. SNPC-70

REPORTED BY Ward C. Roman
Ward C. Roman

APPROVED BY James W. Clark
James W. Clark, Chief
Fluid and Systems Dynamics

DATE September 1970

NO. OF PAGES 73

COPY NO. 28

FOREWORD

An exploratory experimental and theoretical investigation of gaseous nuclear rocket technology is being conducted by the United Aircraft Research Laboratories under Contract SNPC-70 with the joint AEC-NASA Space Nuclear Propulsion Office. The Technical Supervisor of the Contract for NASA is Captain C. E. Franklin (USAF). Results of portions of the investigation conducted during the period between September 16, 1969 and September 15, 1970 are described in the following eight reports (including the present report) which comprise the required first Interim Summary Technical Report under the Contract:

1. Klein, J. F. and W. C. Roman: Results of Experiments to Simulate Radiant Heating of Propellant in a Nuclear Light Bulb Engine Using a D-C Arc Radiant Energy Source. United Aircraft Research Laboratories Report J-910900-1, September 1970.

2. Jaminet, J. F. and A. E. Mensing: Experimental Investigation of Simulated-Fuel Containment in R-F Heated and Unheated Two-Component Vortexes. United Aircraft Research Laboratories Report J-910900-2, September 1970.

3. Vogt, P. G.: Development and Tests of Small Fused Silica Models of Transparent Walls for the Nuclear Light Bulb Engine. United Aircraft Research Laboratories Report J-910900-3, September 1970.

4. Roman, W. C.: Experimental Investigation of a High-Intensity R-F Radiant Energy Source to Simulate the Thermal Environment in a Nuclear Light Bulb Engine. United Aircraft Research Laboratories Report J-910900-4, September 1970. (present report)

5. Bauer, H. E., R. J. Rodgers and T. S. Latham: Analytical Studies of Start-Up and Dynamic Response Characteristics of the Nuclear Light Bulb Engine. United Aircraft Research Laboratories Report J-910900-5, September 1970.

6. Latham, T. S. and H. E. Bauer: Analytical Studies of In-Reactor Tests of a Nuclear Light Bulb Unit Cell. United Aircraft Research Laboratories Report J-910900-6, September 1970.

7. Palma, G. E. and R. M. Gagosz: Optical Absorption in Transparent Materials During 1.5 Mev Electron Irradiation. United Aircraft Research Laboratories Report J-990929-1, September 1970.

8. Krascella, N. L.: Analytical Study of the Spectral Radiant Flux Emitted from the Fuel Region of a Nuclear Light Bulb Engine. United Aircraft Research Laboratories Report J-910904-1, September 1970.

Report J-910900-4

Experimental Investigation of a High-Intensity R-F Radiant Energy Source to Simulate the Thermal Environment in a Nuclear Light Bulb Engine

TABLE OF CONTENTS

TABLE OF CONTENTS (Continued)

Report J-910900-4

Experimental Investigation of a High-Intensity R-F Radiant Energy Source to Simulate the Thermal Environment in a Nuclear Light Bulb Engine

SUMMARY

Experiments were continued to develop an intense radiant energy source capable of producing radiant energy fluxes approaching those expected in a full-scale nuclear light bulb engine. The test program was conducted using the UARL 1.2-megw radio-frequency (r-f) induction heater operating at approximately 5.5 mHz. R-F energy was deposited in an argon plasma discharge contained within a radial-inflow vortex. The 2.24-in.-ID test chamber was formed by concentric, water-cooled, fused silica tubes and a symmetric pair of copper end walls spaced 2 in. apart.

The effects of various geometric, flow and r-f parameters on the power radiated from the plasma, the power deposited in the surrounding water-cooled transparent peripheral wall, and the power convected away from the plasma were investigated. Tests were conducted at pressures up to 19.2 atm. A maximum heat deposition rate per unit volume of 0.57 megw/in.^{3} was achieved in the steady-state, ellipsoidal plasma. The maximum radiant energy flux achieved at the edge of the plasma was 49 kw/sq in. which corresponds to an equivalent black-body radiating temperature (based on the plasma surface area) of 10,860 R. For comparison, the edge-of-fuel radiant energy flux of the full-scale nuclear light bulb reference engine is about 178 kw/sq in.; the corresponding equivalent black-body radiating temperature is 15,000 R.

The results demonstrate the ability to deposit, in a steady-state manner, large amounts of r-f power into a very small plasma. The results also indicate that the total r-f power deposited, the chamber pressure, the argon vortex weight flow rate, and the operating frequency are interrelated in determining stable operating conditions for a given chamber geometry. The maximum levels of plasma power and chamber pressure used in these tests were limited by an instability of the confined plasma similar to instabilities encountered previously at lower powers and pressures. Based on data obtained during this program, it is believed that the instability is related to one or more of these factors: (1) a requirement for

increased end-wall thru-flow port area to prevent choking of one or both ports, (2) r-f breakdown around the end walls due to heating of the argon vortex injectors and secondary flows, and (3) a requirement for operating at lower r-f frequencies to compensate for the changing electrical characteristics of the plasma as power and pressure increase.

Supporting research, including spectral emission measurements of the r-f plasma in the ultraviolet, was conducted. Filament-wound pressure vessels for use in the nuclear light bulb research program were also developed and tested.

RESULTS AND CONCLUSIONS

1. The maximum plasma power density achieved was 0.57 megw/in.^{3} and was obtained at an absolute steady-state power deposited into the plasma of 160 kw. This occured at the highest chamber pressure, 19.2 atm, and represents an increase of approximately 75 percent over the maximum power density achieved previously.

2. The maximum steady-state power deposited into the plasma was 223 kw. The corresponding diameter of the plasma, measured at the axial midplane, was 0.75 in. The maximum power radiated through the inner water-cooled transparent wall was 162 kw.

3. The maximum radiation flux achieved, based on the surface area of the plasma, was 49 kw/sq in. which is equal to the flux from a black-body radiating at 10,860 R. This steady-state flux represents an increase of approximately 30 percent over the maximum level achieved previously. The increase is due primarily to the smaller-diameter plasmas and higher power densities obtained.

4. The r-f operating frequency, the total power deposited into the plasma, the chamber pressure, and the argon weight flow rate are interrelated in determining the most stable operating conditions for a given geometry. Simultaneous increases in chamber pressure and r-f power into the plasma yielded the largest increases in the radiation efficiency, i.e., the largest increases in the fraction of the total power deposited into the plasma that was radiated through the inner transparent wall. Radiation efficiencies reached about 85 percent at chamber pressures close to 20 atm.

5. The maximum levels of power deposited into the plasma and of chamber pressure in these tests were limited by an instability which repeatedly caused the plasma to relocate around one or the other of the end walls. Similar instabilities were noted previously at lower powers and pressures. To obtain further increases, the following factors that could cause this instability must be investigated: (1) the possibility that one or both end-wall thru-flow ports are becoming choked, requiring increased thru-flow port area, (2) the possibility that heating of the argon vortex injectors and secondary flows around the end walls lead to local r-f breakdown, and (3) the possibility that the changing electrical characteristics of the plasma require lowering of the r-f operating frequency as power and pressure increase.

6. The plasma diameter at the axial midplane decreased with increasing argon weight flow rate (weight flow rates from 0.010 to 0.035 lb/sec were used) and, to a lesser extent, with increasing chamber pressure and decreasing r-f frequency. The plasma could be maintained in a relatively laminar, stable ellipsoidal geometry with diameters from about 0.5 to 0.75 in.

7. Approximately 90 percent of the total power deposited into the water-cooled copper end-wall assembly was due to conduction and convection from the flow as it was exhausted through the thru-flow ducts from the vortex chamber. The fraction of the total discharge power that was deposited into the face of the end walls was about 0.06.

8. Radial distributions of temperature determined spectroscopically from continuum measurements at a wavelength of 4320 Å indicate that a distinct off-axis peak in temperature occurred at approximately mid-radius. Plasma centerline temperatures ranged between about 20,500 and 21,500 R, while the off-axis peak values were approximately 5 percent higher.

INTRODUCTION

An experimental and theoretical investigation of gaseous nuclear rocket technology is being conducted by the United Aircraft Research Laboratories under Contract SNPC-70 administered by the joint AEC-NASA Space Nuclear Propulsion Office. This research is presently directed toward the nuclear light bulb engine concept. Details of this concept are discussed in Refs. 1 through 5. The concept is based on the transfer of energy by thermal radiation from fissioning gaseous nuclear fuel, through an internally cooled transparent wall, to seeded hydrogen propellant flowing in an annulus surrounding the transparent wall. The hydrogen propellant is seeded with sub-micron particles to increase its opacity.

Figure 1(a) illustrates this concept and principle of operation. The reference engine (Ref. 1) consists of a cluster of seven such cavities. A transparent buffer gas (neon) is injected tangent to the inner surface of the transparent wall to form a radial-inflow vortex (Refs. 2 and 6) which serves to contain the gaseous fuel and isolate it from the transparent wall. This type of vortex exhibits well-defined recirculation cells with a radial stagnation surface (i.e., a cylindrical surface across which there is no flow in the radial direction) at a large radius. The purpose of the neon buffer gas is to prevent diffusion of the nuclear fuel to the wall. The gas discharged from the unit cavities contains nuclear fuel and fission products. The fuel is condensed, centrifugally separated from the neon, and pumped back into the fuel-containment region of the vortex. The neon is further cooled and pumped back into the cavity to drive the vortex. High purity, internally cooled, fused silica tubes (tube wall thickness of approximately 0.005 in.; Ref. 7) appear suitable for the transparent wall. Because of the high temperature obtainable in the gaseous fuel, nuclear light bulb engines can theoretically provide specific impulses greater than 3000 sec and thrust-to-weight ratios greater than one (Ref. 8). In addition, this closed-cycle fuel system concept offers the possibility of providing perfect containment of gaseous nuclear fuel and fission products.

Determination of the feasibility of a nuclear light bulb engine requires research in a number of technological areas including fluid mechanics, heat transfer, nuclear criticality and engine dynamics, and transparent-wall structure fabrication techniques. The research discussed in this report was directed at developing a non-nuclear r-f plasma radiant energy source that will provide steady-state radiant energy fluxes similar to those expected in a full-scale engine. Recent investigations related to other areas of the nuclear light bulb engine are reported in Refs. 7 and 9 through 14.

Figure 1(b) shows the r-f plasma radiant energy source geometry. The desired plasma source has a length of 2 in. (major axis) and a diameter of approximately 0.5 in. (minor axis). The transparent peripheral walls of the test chamber are concentric, water-cooled, fused silica tubes. A symmetric pair of water-cooled copper

end walls form the ends of the test chamber. The significant length dimensions of the engine cavity and the r-f plasma radiant energy source are shown in Fig. 1. To establish the required radial-inflow vortex flow pattern, argon was injected through vortex injectors located on each end wall. Each end wall contains a thru-flow port on the centerline to remove the argon gas from the vortex chamber. The 1.2-megw induction heater provided the r-f energy for the argon plasma which was contained within the vortex flow. The r-f plasma occurs in the region between the end walls with the major axis colinear with the thru-flow port axis.

The primary objectives of the research reported herein were to increase the power deposited in the plasma and increase the operating pressure, thereby increasing the radiant energy flux. This work involved investigation of the effects of various geometry, flow and r-f parameters on the power radiated from the plasma, the power deposited in the surrounding water-cooled transparent peripheral wall, and the power convected away from the plasma. Other work accomplished included supporting research on the use of filament-wound pressure vessels in future high-pressure tests involving r-f plasma and early in-reactor simulation testing (Appendix A), and spectral emission measurements, from 0.15 to 0.43 microns, of the r-f plasma (Appendix B).

DESCRIPTION OF PRINCIPAL EQUIPMENT

UARL 1.2-Megw R-F Induction Heater

Background

The experiments described in this report were conducted using the UARL 1.2-megw r-f induction heater. This heater was constructed during 1966 and 1967 as part of the UARL Corporate-sponsored program. The heater was designed to ultimately be capable of depositing approximately 0.6 megw of r-f power into a relatively small plasma discharge. In its present configuration, the heater has deposited steady-state about 0.22 megw of r-f power into a 0.58-in.^{3} plasma discharge. Corporate-sponsored tests employing a salt-water load (uniform electrical conductivity) have continued to further develop and check out operation of all r-f induction heater components. During these tests, up to 0.31 megw was deposited into the salt-water load. The overall system efficiency, defined as total r-f power deposited in the load divided by the total d-c power supplied to the heater, was about 45 percent.

Primary Heater Components

A detailed description of this equipment is given in Ref. 15. A block diagram showing the primary components of the heater is presented in Fig. 2. The r-f output power is supplied by two power amplifier tubes which drive a resonant tank circuit (resonator section) of unique design. The operating frequency is selected by means of a variable-frequency oscillator. The r-f operating frequency is approximately 5.5 mHz. The power levels noted in Fig. 2 correspond to the maximum rated r-f output for each component. The approximate 0.5-w output of the variable frequency oscillator is increased in stages with a sequence of r-f power amplifiers to an intermediate power level of 80 kw at the output of the buffer amplifier. This power level is further increased to 880 kw using a pair of power amplifier tubes connected in a push-pull configuration. The category of operation of the final amplifier stage is class "C". Voltage levels noted on Fig. 2 correspond to the maximum rated d-c voltage input for the various amplifiers. The maximum total d-c input power to the power amplifiers employed in plasma discharge tests during this program was about 650 kw. The heater has been operated with a salt-water (mock-up) load at input d-c power levels exceeding 750 kw.

The resonator section (part of which is visible in Fig. 3) consists of two arrays of ten vacuum capacitors. The ends of the capacitors are water-cooled and r-f chokes are installed in the cooling water lines. The resonator section and test section (load) are located within a large (approximately 5-ft-dia) cylindrical aluminum test tank. The front dome of the test tank contains five 4-in.-dia fused silica windows which allow observation of the test chamber from different angles.

In addition, a double mirror arrangement located inside the test tank allowed viewing of the top and bottom of the test section. Each resonator section is connected to a single-turn work coil (see Fig. 3). The two single-turn work coils each consist of five water-cooled 0.187-in.-dia copper tubes. The copper tubes were silver soldered together to form a single structure. The coils are 3.06 in. in diameter and were silver plated to reduce resistive heating due to the high coil current.

Figure 4 is a photograph of the control consoles used in the radiant energy source tests. The power control console for the r-f induction heater is shown at the right. The saturable reactor power control is used to vary the d-c voltage supplied to the power, buffer and driver amplifiers (see Fig. 2). In addition to the voltage, current, and power meters shown above the console, strip-chart recorders were used during tests for continuously monitoring the r-f induction heater power characteristics. Adjacent to the induction heater power control console is the r-f heater cooling system monitoring and control console. The oscillator-driver control console contains the variable frequency oscillator, neotron amplifier stages, and controls for tuning the matching circuit at the final power amplifier input. This allows individual adjustment to be made to the various amplifier systems, thus aiding in increasing overall system efficiency. The frequency counter shown in Fig. 4 is used to monitor the r-f operating frequency. The radiant energy source control console contains the gas, cooling water, and starting system controls and associated monitoring equipment. A set of single and dual strip-chart recorders (approximately 0.5-sec response time) and an automatic stepping temperature recorder were used to permit simultaneous monitoring of the various critical measurements during the tests. The r-f input power to the discharge is determined by the r-f voltage supplied to the resonator section of the heater (Fig. 2) and the impedance of the plasma (related to the electrical conductivity and plasma size) and resonator which, in turn, determines the current level. The r-f voltage applied to the resonator section was measured with a capacitive-type voltage probe.

Radiant Energy Source Test Chamber and Related Systems

Test Chamber

Figure 3 is a photograph of the test chamber and r-f induction heater resonator section (including the r-f work coils). This section of the system is described in Ref. 15. A pair of concentric water-cooled fused silica tubes, approximately 39 in. long and located concentrically within the r-f work coils, form the outer boundary of the test chamber (the location of the inner fused silica tube is shown by the dashed line in Fig. 3). The nominal dimensions of the outer and inner fused silica tubes are 2.54-in.-ID by 2.88-in.-OD and 2.24-in.-ID by 2.38-in.-OD, respectively. The annulus between the tubes was used for water coolant. To reduce the intense radiation from the source incident on the components within the aluminum test tank,

known concentrations of an organic, water-soluble dye (nigrosine CI-50420) were added to the test-chamber cooling water. The cooling manifolds for the resonator section and r-f work coils are also shown in Fig. 3. Also noted is the typical location of the plasma discharge region.

Gas System

Figure 5 is a block diagram of the argon gas injection and exhaust system. Argon was injected into the test chamber through vortex injectors located on each end-wall assembly. The argon was supplied from an 11-bottle argon supply (2500 scf capacity). This permitted long-run-time capability, particularly during tests at high power with high argon weight flow rates. Rotameters were used to measure the argon weight flow rate during most of the low-pressure tests. For tests at chamber pressure above 8 atm, a sonic orifice flow metering system was used (see Fig. 5). Water-cooled flow control valves (coarse and fine flow control) were located at the exit of each thru-flow duct to permit independent control over the argon weight flow rate through each thru-flow port.

Plasma Starting System

A d-c arc was used to start the r-f plasma discharge. A detailed discussion of the starting system is given in Ref. 15. Basically, a low-power d-c arc is drawn between two movable electrodes inserted into the thru-flow ports. The d-c arc is maintained until the amount of r-f power deposited in the arc plasma is sufficient to sustain the r-f plasma in the test chamber. The starting time is approximately 10 msec. This system permitted r-f plasmas to be started at chamber pressures of approximately one atmosphere (sometimes higher).

Water-Cooling Systems

To provide the necessary cooling, two closed-loop water cooling systems, each with a total capacity of approximately 75 gal, are used. A low-pressure system employing centrifugal pumps can supply up to 100 gpm of cooling water at 180 psig. A high-pressure system using a positive displacement pump supplies up to 20 gpm of cooling water at 450 psig. In addition, to reduce the pressure pulsations inherent in positive displacement type pumps, a high-pressure surge accumulator is used to damp out the pressure pulsations to less than one percent. Two large, open-top, stainless steel tanks (70 gal capacity) act as the storage reservoirs for each coolant loop.

Diagnostic Equipment

Total Radiation Measurements

The power radiated from the plasma was measured using a specially constructed radiometer and chopper wheel assembly. Details and sketches of the radiometer system and calibration method are described in Ref. 15. The transmission characteristics of the radiometer optical system and various filters are shown in Fig. 6(a). A Reeder RBL-500 thermopile detector with a BaF_2 window was used as the radiometer sensing element. The output of the thermopile was connected to an operational amplifier and displayed either on an oscilloscope or on a strip chart. Internal r-f shielding and r-f chokes were used to isolate the radiometer electronic system. For the tests reported herein, total radiation was determined in the following wavelength bands: 0.25 to 1.3, 0.3 to 1.3, 1.0 to 1.3, and 0.72 to 1.3 microns. As illustrated in Fig. 6(a), these wavelength cut-offs were determined by the 50-percent transmission levels of the individual filters in the radiometer, the 50-percent transmission level of the 0.079-in.-thick annular cooling water layer located between the two fused silica tubes within the test chamber (Fig. 3), or the BaF_2 window. The 50-percent transmission level of the cooling water layer was calculated from the absorption coefficients for pure water given in Ref. 16. Figure 6(b) shows a typical oscilloscope trace of the thermopile output signal in millivolts in the various wavelength bands as a function of time. A General Electric (DXW) tungsten filament lamp was used as the reference source. The response of the radiometer system with filters was calibrated using a Eppley Laboratory Calibrated Standard of Spectral Irradiance. The total power radiated from the plasma was calculated assuming isotropic radiation, including allowance for blockage due to the r-f work coils.

As discussed in the previous section, nigrosine dye (CI-50420) was used to reduce the intense radiation from the r-f plasma radiant energy source by adding known dye concentrations to the test chamber cooling water. Nigrosine was selected after tests were conducted to determine the type of dye or pigment with the most desirable characteristics (see Ref. 15). In addition, tests were conducted to verify that the absorption characteristics of the coolant with nigrosine added were not influenced by radiation from the plasma source or by the bulk temperature of the coolant for the range of test conditions employed. Results of other tests showed the water-dye coolant in the concentrations used absorbed negligible amounts of r-f energy, thereby introducing no errors into the energy balance calculations. Figure 7 shows the radiation attenuation obtained using a range of concentrations of nigrosine dye-water. The solubility of nigrosine dye in water is approximately 1.0 lb/lb at 175 F (Ref. 17). Nigrosine dye in concentrations varying from 100 to 1000 ppm (on a weight basis) was used during the tests.

Optical Scanning System for Determination of Plasma Diameter

The basic system includes a head-on photomultiplier tube, a fiber optic tube, and a collimating tube containing two apertures and associated baffles attached to a traversing mechanism powered by a synchronous motor. The output from the phototube went to a signal conditioner and then to a strip-chart recorder. The fiber optic tube and traversing mechanism were located on a central view port of the experimental test tank to permit scans of the discharge diameter at the axial midplane. A 1.0-percent cut-off criterion (i.e., the intensity equal to 1.0 percent of the peak intensity; see Ref. 15) was used for establishing the discharge diameter from the scanner trace; agreement within about 5 percent of the diameter determined from photographs using various neutral density filters was obtained. Additional details and sketches of the fiber optic scanning device are given in Ref. 15.

Viewing System for Observing Plasma Behavior

Continuous observation of the radiant energy source during the tests was accomplished using a projection screen system. An 18-in. focal length convex lens and neutral density filter system was used to project an image of the plasma radiant energy source onto an overhead viewing screen. Horizontal and vertical grid lines were placed on the screen; this allowed continual visual observation of changes in plasma geometric characteristics. In addition, a set of swivel-base mirrors were attached to each side view port on the test tank; this permitted continuous observation of the end regions of the plasma and the condition of the end-wall faces and thru-flow ports.

Photographic Equipment for Plasma Size, Shape, and Stability Observations

High-speed movies (framing speeds up to 8,000 frames per sec) and still pictures taken from several of the view ports permitted an estimation to be made of the discharge size, shape, and volume. Because a portion of the discharge region was always shielded from view by one or both of the r-f work coils, only an approximation to the true discharge volume could be obtained from the photographs.

Spectral Emission Measurements

The optical system used to obtain spectral emission measurements is described in detail in Ref. 15. The same Jarrel-Ash 0.25-meter Ebert Monochromator was used to obtain the chordwise scans of the discharge at the midplane. The monochromator had 25-micron-wide entrance and exit slits. A calibrated 13.5-in. focal length lens was positioned between the r-f plasma radiant energy source and the entrance slit of the monochromator. The lens center was 26.5 in. from the plasma source major axis.

The lens was positioned such that the image was projected on the entrance slit of the monochromator resulting in a magnification factor of 1.41. The lens location reported in Ref. 15 resulted in a magnification factor of 1.0. Scans were made of the continuum at 4320 Å by traversing the monochromator through the image at the axial midplane. The scanning rate was 5 in./min. The continuum at 4320 Å was selected to obtain the spectral emission measurements over the 4158.59 Å line as reported in Ref. 15. There were several reasons for this. The 4320 Å continuum represents the best documented continuum region of an argon plasma (Refs. 18 and 19). The possible influence of line broadening and self-absorption, particularly at the higher pressure and power regime is uncertain for the 4158.59 Å line. When looking at a particular line using the diagnostic equipment available, it was not possible to determine exactly how much the line width changes as a function of increasing chamber pressure and total discharge power. Based on this, it is expected that increased accuracy in determination of the radial distributions of temperature should result using the continuum at 4320 Å. Various calibrated neutral density filters were located in front of the monochromator entrance slit to reduce the intensity of the incident light corresponding to different test conditions. Unfortunately, the presence of the concentric fused silica tubes with the coolant annulus and several mirrors located within the test tank may have some influence on the accurate determination of intensity. Reflections from the more intense sections of the plasma within the test chamber off these various surfaces may introduce possible errors. The photomultiplier output went into a signal processor and was then displayed on a strip-chart recorder modified to operate at a high feed rate (30 in./min). The strip-chart recorder replaced the visicorder used in Ref. 15. This helped significantly to damp out the high-frequency (360 Hz) oscillations recorded on the visicorder in the earlier tests. These distinct periodic fluctuations in intensity were attributed to the 360 Hz ripple frequency of the three-phase power supply. In some tests, these accounted for up to 30 percent fluctuation in signal intensity. This same basic optical equipment was used, subject to minor modifications, in the spectral emission measurements of the r-f argon plasma discussed in Appendix B.

Calorimetric Measurements

Measurements were made of all cooling water flow rates using rotameters with the sole exception of the water-dye coolant loop. In this case it was necessary to use calibrated magnetic-type flowmeters. The associated inlet and exit coolant temperatures were monitored with copper-constantan thermocouples located as close to the test region as possible. As discussed previously, the power convected out the thru-flow port exhausts was measured using calorimeters installed in each of the two separate exhaust lines.

Description of Test Configurations

Vortex Injector End-Wall Configuration

The radiant energy source test chamber used in the 1.2-megw r-f induction heater tests was described previously; Fig. 3 is a photograph of the test chamber. Figure 8(a) is a sketch of the radiant energy source configuration having 16 vortex injectors per end wall that was used in the tests reported herein. The configuration consists of a symmetrical pair of cylindrical, 0.80-in.-dia, water-cooled copper end walls spaced 2.0 in. apart. These end walls are located concentrically within the fused silica tubes and form the axial boundary of the plasma in the test chamber. To aid in increasing their reflectivity, the faces of each end wall were lapped and highly polished using a series of abrasive pastes followed by aluminum powder. The results of separate tests conducted using the actual polished end walls indicated between 70 to 75 percent of the total radiation incident on the highly polished copper end-wall face in the wavelength band from 0.25 to 1.3 microns was reflected. The total radiation from the d-c arc used as a source for these measurements within the wavelength band of 0.25 to 1.3 microns is similar to that from the r-f radiant energy source.

Figure 8(a) also shows the 0.185-in.-dia thru-flow ports for removing the argon test gas from the test chamber and the passages which provide the meridional flow of cooling water at the end-wall face and along its axis. This cooling water flow pattern should permit the greatest temperature difference across the end-wall face in addition to taking advantage of centrifugal effects in the annular region near the end-wall face. The end-wall cooling passages were sized to provide the maximum flow velocities near the end-wall face and along the inner annulus surrounding the thru-flow duct (locations where high local heat fluxes are expected).

To establish the desired radial-inflow vortex flow pattern, argon is injected at each end wall through 16 0.067-in.-ID stainless steel vortex injectors. It is through this fluid dynamic technique that control of the plasma has been effectively achieved with the edge of the discharge confined well away from the inner transparent peripheral-wall boundary (see plasma location in Fig. 8(a)). One set of 8 injectors forming the outer set are located equally spaced around a circle with a diameter of 1.87 in. The inner set of 8 injectors are similarly positioned, but on a diameter of 1.19 in. (see Fig. 8(a)). The exit plane of the vortex injector manifold was 2.25 in. back from the face of the end wall.

Figure 9 shows more details of the multiple vortex injector manifold having 16 vortex injectors at two radial locations. The injectors were set at an angle of 11 deg from the circumferential direction (see "Section B-B" in Fig. 9); this provided an axial component to the injected flow. The injectors were also set at an angle of 30 deg radially inward from the circumferential direction (see "face"

view in Fig. 9). The stainless injectors were silver-soldered into a water-cooled copper manifold. Independent feed lines were used to route the argon gas to the inner and outer set of injectors. Separate manifolds were employed to allow investigation of the effect of changing the injection from both manifolds simultaneously to either the inner or outer set only. Figure 9 shows the approximate locations of temperature sensitive paint used in several preliminary tests to determine the temperature reached due to r-f heating effects only (no plasma present). During some early hot-flow tests with the plasma present, temperature sensitive paint was also used at these points to verify the manifold water-cooling effectiveness.

For comparison, Fig. 8(b) illustrates the configuration used in tests described in Ref. 15. This configuration had only 8 0.10-in.-ID stainless steel vortex injectors on each end wall, all located on a 1.44-in.-dia circle. The exit of the vortex injector copper spacer ring using this configuration was 2.86 in. back from the face of the end wall. The same basic water-cooled copper end wall assembly was used. However, the symmetric configuration employing 16 vortex injectors on each end wall at the two radial locations provided better fluid-dynamic control of the plasma over the test range. Part of this improvement may have resulted from the fact that the injectors and their manifolds were located closer to the plasma; this reduced the overall volume of the chamber exposed to the vortex flow. In addition, the copper spacer shown in Fig. 8(b) had an annular gap of about 0.2 in. between it and the inner fused silica tube; this exposed more total volume (including volume behind the end walls) to the vortex flow and resulted in additional dissipation of the strength of the vortex.

The range of injection Reynolds number $Re_{t,j}$ for the tests reported herein was from about 8×10^4 to 2×10^5; in previous cold-flow tests (Ref. 20), stable vortex flow patterns were observed in this range. The argon injection velocities used in the tests reported herein ranged between about 20 and 100 ft/sec.

Calculations and static tests were presented in Ref. 15 to estimate the stress limits in the inner and outer fused silica tubes used in the test chamber. The calculations included both hoop and thermal stresses. The results indicated that, by using the basic test chamber configuration shown in Fig. 3, relatively high powers (approximately 250 kw) and pressure levels (approximately 20 atm) could be achieved while maintaining a reasonable factor of safety. Table I is a summary of the specific properties of the fused silica tubes used in the tests reported herein. The hoop stresses at failure (no thermal stress) are indicated at the bottom of the table; these are based on measurements reported in Ref. 15. Using the stresses shown in Table I, the factor of safety in these tests was about 4.

Experiments related to the use of the 1.2-megw r-f induction heater for future simulated propellant heating tests were conducted using a configuration similar to that described in Ref. 15 (Fig. 38). For these tests the source was located within

a 1.06-in.-ID concentric coolant-tube transparent wall model. A simulated propellant heating duct (0.56-in. annulus) surrounded the transparent wall model. In these tests various propellant stream and radiant energy source test conditions were employed. Carbon was used as the seed material. Because of the horizontal orientation of the propellant duct and reduced propellant duct annular dimensions compared with those used in the tests of Ref. 9, the average propellant stream velocity used was higher (10 to 35 ft/sec) than in the d-c arc propellant heating tests (5 ft/sec). The hot-flow propellant heating tests conducted, using argon or helium gas at pressures from 1 to 2 atm, resulted in electrical breakdown and arc-over in the propellant duct. Both azimuthal-type and axial filament-type discharges occurred. Results of additional tests indicated the cause of the breakdown and arc-over to be related to the presence of the carbon seeds (partial accumulation on the duct walls and relatively large size particles in the duct).

To complement the experiments, an analysis of the possible arc-over and breakdown phenomenon that might occur due to the present r-f coil configuration, r-f test conditions, and propellant heating test conditions was conducted. The calculated results indicated possible breakdown could occur due to (1) strong E_z fields, (2) large size particles within the duct and (3) high particle number density locally within the duct. However, the size and distribution of the carbon particles within the propellant duct is the primary unknown at the present time.

The results of these experiments and calculations indicate future propellant heating tests using the 1.2-megw r-f induction heater are feasible, provided solutions to the problem of electrical breakdown and arc-over are found. Solution of these problems might require use of nonconducting seed materials with increased deagglomeration, shielding techniques to minimize or eliminate the E_z field, and/or a modified r-f work coil and propellant duct geometry. The success of the propellant heating tests using the d-c arc, as reported in Ref. 9, precluded additional tests to investigate the various alternatives. As required in the future, additional tests can be conducted using the 1.2-megw r-f radiant energy source for heating a seeded simulated propellant to high exit temperatures.

DESCRIPTION OF TEST PROCEDURES AND DATA-ANALYSIS METHODS

Test Procedures

The sequence of events occurring during a typical test is presented in Table II. Measurements of important electrical quantities, cooling water flow rates, and associated temperature rises in critical parts of the induction heater system were made during selected tests to provide information required for performing a component and overall system energy balance. It should be emphasized that to maintain a relatively steady, stable discharge, the combination of total discharge power, chamber pressure, argon weight flow rate, and r-f operating frequency are interrelated for the given configuration tested. Simultaneous changes in at least two of these parameters was usually necessary to maintain a steady and stable plasma.

The primary independent variables in the radiant energy source tests reported herein are the r-f operating frequency, the chamber pressure, the argon weight flow rate, the d-c input power, and the geometry. The primary dependent variables are the discharge diameter (size and shape), total discharge power, power radiated from the plasma discharge, power lost by conduction, and the radial distribution of temperature within the discharge. Secondary dependent variables would include those that are temperature-dependent (e.g., electrical conductivity and thermal conductivity). The coupling and interactions between the plasma discharge and the high frequency magnetic fields which produce the discharge are most complex. Theories related to r-f plasma discharges make numerous simplifying assumptions related to the plasma boundary conditions and conductivity profiles (see Refs. 21 and 22); no theory includes one of the more important effects, convection. The electrical and thermal characteristics of vortex stabilized r-f plasmas strongly depend on this mechanism of heat dissipation. The shape, size and stability of the discharge also depend on the effects of convection, in addition to the interaction between the plasma and the fields of the r-f work coils. Where possible, throughout this test program, several of the independent variables were held as constant as possible to permit a systematic comparison to be made and important trends noted. However, as higher pressures and discharge powers are reached and minor changes in basic configurations are made, new effects may occur or even dominate the influence on various parameters.

Determination of Source Diameter

The plasma diameter at the axial midplane, d, was determined using the optical scanning system. It should be emphasized that the strong radial variations of temperature for an r-f argon plasma (particularly the high gradients at the edge of

the plasma discharge) make it difficult to define a true discharge diameter. The temperature distribution within the plasma is determined by the balance between the generated and dissipated energy. Under steady-state conditions, the thermal energy generated by ohmic heating within the r-f plasma must be dissipated to the environment by the various transport processes, e.g., thermal conduction, convection, and radiation. These processes constitute an extremely complex energy exchange system which can be solved analytically only for very simple cases. A further complication is that the dominating gas properties are also strong functions of the temperature which itself varies across the r-f discharge. From the standpoint of determining a discharge diameter, the criterion established in Ref. 15 was used. The diameter determined in this way should correspond to a boundary temperature of approximately 14,000 R. At this temperature, the electrical conductivity has decreased by greater than one order of magnitude from the value corresponding to the maximum temperatures of the r-f plasma discharge as measured in this investigation (see later discussion). By selecting and defining the discharge diameter based on this criterion, a systematic comparison of the influence of various parameters on the discharge diameter can be made.

Determination of Source Energy Balance

Figure 10 is a sketch of the radiant energy source showing the power breakdown. The total power deposited into the radiant energy source, Q_T, was obtained from an overall energy balance. Figure 10 shows the various power loss mechanisms and the measurement techniques used in determining them. The power radiated from the source which passed through the fused silica tubes and water-dye coolant was measured with the radiometer system described in the Diagnostic Equipment Section. By monitoring the flow rate and associated temperature rise of the coolant flowing in the annulus between the inner and outer fused silica tubes, the total power deposited in the peripheral wall, Q_W, was calculated. Similarly, by monitoring the flow rate and associated temperature rise of the coolant flowing in each end wall, the total power deposited in the end walls, Q_E, was determined. Water-cooled calorimeters attached to each end-wall thru-flow port exhaust permitted determination of the amount of power that was convected out the thru-flow exhausts (Q_L). The total power deposited in the r-f plasma discharge was then obtained from

$$Q_T = Q_R + Q_W + Q_E + Q_L \qquad (1)$$

Determination of Source Radiation Characteristics

Total Power Radiated and Radiant Energy Flux

To permit calculations of the radiant energy flux at the surface of the discharge, the total radiated heat transferred through the inner fused silica tube of the test chamber must be obtained. For the data reported herein, this total radiated heat transferred through the inner fused silica tube, $Q_{R,T}$, is defined as $Q_{R,T} = Q_R + Q_W - Q_C$ where Q_R is the radiated power, Q_W is the power deposited in the peripheral-wall coolant, and Q_C is the power conducted through the inner fused silica tube. Since Q_C was not measured directly, estimates of Q_C were made by calculating the maximum heat flux which could be conducted through the inner fused silica tube for the range of test conditions reported herein. This estimate was based on experimental test experience (Ref. 15) and careful examination of the inner fused silica tubes (both before and after hot-flow tests). For the tests reported herein, no traces of residual thermal stress were found when viewing the tubes under polarized light after exposure to high radiant energy flux conditions. Thus it was assumed that the inner surface of the peripheral wall did not exceed 1500 R. This assumption is reasonable, since there were no indications of severe local heating of the peripheral walls or boiling of the water-dye coolant in the annulus for any of the tests reported herein. This assumed inner wall maximum surface temperature is approximately 30 percent less than the value assumed in Ref. 15 and is based on the reduced plasma discharge diameter obtained and the absence of any thermal stress. As in Ref. 15, it was further assumed that the effective surface area for conduction heat flow is governed by the periphery of the inner fused silica tube over an axial length of about 3.0 in. The discharge major axis is 2 in. Based on previous test experience and separate radiant energy source heating tests conducted using temperature sensitive paint at various locations in the test chamber, it was estimated that convective heating of the inner fused silica tube occurs over approximately a 3-in. length. Then, using the thermal conductivity relationship with temperature for fused silica reported in Ref. 7, the maximum Q_C was estimated to be equal to about 7.5 kw. It was assumed that the power conducted through the inner fused silica tube would decrease as the total discharge power and argon weight flow rate decrease. The argon weight flow rate was not changed over a wide enough range to significantly alter the heat transfer coefficient (dependent on 4/5th power relationship); therefore as a first approximation, it is reasonable to assume Q_C varied approximately linearly with Q_T. This relationship was used in calculating the values of $Q_{R,T}$. The decrease in discharge diameter corresponding to the decrease in total discharge power and argon weight flow rate would also tend to further reduce Q_C. In addition, several tests were conducted with heavy concentrations of dye in the coolant water; these tests also verified that a large fraction of the energy deposited in the annular coolant was due to radiation.

Power Density

Calculations of the power density Q_T/V, were made using the total discharge power, Q_T, determined from the overall power breakdown (see Fig. 10) and the discharge volume determined from calculations based on the measured source diameter (the discharge was assumed to be ellipsoidal).

DISCUSSION OF RESULTS

Factors Which Influence Source Diameter

Total Discharge Power, Argon Weight Flow Rate and Chamber Pressure

Figure 11 illustrates the effects of varying the total discharge power on the geometric characteristics of the discharge. Data are shown both for the latest test configuration (shown in Fig. 8(a)) and the data from Ref. 15 using the earlier test configuration (shown in Fig. 8(b)). The range of chamber pressure, argon weight flow rate, and r-f operating frequency are shown in Fig. 11. Note that the chamber pressure ranged over about one order of magnitude, from 2 to 19.2 atm. A range of about a factor of three in argon weight flow rate (0.010 to 0.035 lb/sec) was used, while the r-f operating frequency shift covered a range of 36.2 kHz (5.5629 to 5.5991 mHz). Data are shown for total discharge power levels, Q_T, up to the maximum achieved in the tests reported herein, 223 kw. For reference, the upper two horizontal dashed lines show the inside diameter of the r-f work coils and the inside diameter of the inner fused silica tube of the test chamber.

The discharge was maintained in a relatively steady, stable geometry with diameters ranging between about 0.50 in. and 0.75 in. A detailed summary of the experimental results shown in Fig. 11 for the configuration having 16 vortex injectors per end wall is presented in Table III. The significantly smaller discharge diameters obtained in these tests is believed to be due to (1) the new vortex injector geometry which reduced the total test volume and moved the injectors and manifolds closer to the discharge and (2) the use of lower r-f operating frequencies which still permitted a steady and stable discharge to be obtained.

For a fixed chamber pressure and relatively constant total discharge power level, the discharge diameter decreased as the argon weight flow rate was increased. The influence of small changes in chamber pressure was a secondary effect; significant increases in chamber pressure resulted in a smaller discharge diameter.

It was difficult to determine the sole influence of a change in only one variable on the others; however, general trends could be obtained. Increasing the total discharge power with all other parameters relatively constant resulted in an increase in discharge diameter.

There are definite limits to the range over which combinations of these parameters can be varied. For example, relatively large diameters (approximately 1 in.) could be obtained by decreasing the argon weight flow rate significantly; however, unsteady discharge behavior resulted. The discharge boundary appeared turbulent and difficult to define. In contrast, increasing the argon weight flow rate resulted in

a smaller discharge up to the point of discharge extinguishment. Extinguishment takes place without any visual warning that it is about to occur. The test conditions for extinguishment are quite repeatable. Apparently the total power deposited into the discharge is not sufficient at those particular operating conditions to sustain a discharge. This situation is also influenced by a drop in coupling efficiency at the smaller plasma diameters. This same extinguishment phenomenon was observed to occur when, at fixed test conditions, the total discharge power was reduced by decreasing the saturable reactor control (see Fig. 4). Again, the total discharge power needed for sustaining a discharge was not maintained, and extinguishment occurred. See later section entitled Results of Exploratory Tests Directed Toward Further Increases in Pressure and Power for additional discussion.

High-speed 16 mm color movies taken of the discharge through several of the view ports were used in establishing the shape of the discharge. The films also verified the symmetry of the discharge relative to the end walls and major axis. Based on the films, an ellipsoidal shape was indicated. Assuming an ellipsoidal shape for the discharge, the discharge surface area and volume were computed using the axial midplane diameter of the discharge as the minor axis of the ellipsoid. The surface area and volume of an ellipsoid of corresponding diameter (minor axis) and 2-in. major axis are also indicated in Fig. 11. These areas and volumes were used in computing the radiant energy fluxes and power densities.

R-F Operating Frequency

The effect of varying the r-f operating frequency on the discharge geometric characteristics and power deposition is illustrated in Fig. 12. During the tests reported in Ref. 15, the r-f operating frequency was set about 25 kHz above the unloaded resonant frequency (i.e., the resonant frequency without the discharge present). In these earlier tests, no attempts were made to shift the r-f operating frequency during operation. Data are shown in Fig. 12 for r-f operating frequencies ranging from 5.5610 to 5.6140 mHz (a bandwidth of 53 kHz). The configuration having 16 vortex injectors per end wall (Fig. 8(a)) was used. The total discharge power was approximately 15 kw, the chamber pressure was 4 atm, and the argon weight flow was held constant at 0.008 lb/sec. For reference, the unloaded resonant frequency and approximate loaded resonant frequency (corresponding to the maximum in resonator voltage) are shown on the abscissa by the vertical dashed lines. A decrease in the r-f operating frequency resulted in a reduction in the discharge diameter. Note the change in discharge diameter of approximately 70 percent obtained over the entire frequency range tested (Fig. 12). For these test conditions and at operating frequencies below about 5.5610 mHz, the discharge always extinguished (see discussion preceding section). At frequencies above about 5.6100 mHz, the discharge developed radial and axial pulsations and gradually changed shape from the ellipsoidal geometry toward a more spherical geometry (with the axial extremities of the discharge withdrawn

away from the end-wall faces); this was followed by a rapid relocation of the discharge onto one or the other of the end walls (also see discussion in section entitled Results of Exploratory Tests Directed Toward Further Increases in Pressure and Power). The approximate frequency range for steady discharge conditions, for the range of test conditions shown in Fig. 12, lies between about 5.5685 and 5.5810 mHz. At frequencies below this level, the discharge was very sensitive to any changes in the test conditions, and unless extreme care was taken in fine adjustment to the independent parameters, discharge extinguishment would occur. At r-f frequencies above 5.5810 mHz, some random radial and axial pulsations developed, and the discharge did not possess a steady, laminar-appearing boundary.

The variations with frequency of other important electrical parameters are also shown in Fig. 12. The resonator voltage (zero-to-peak) is the r-f voltage present in the resonant tuned output circuit of the r-f induction heater (as measured with a capacitive voltage-dividing probe). Note that the peak value of resonator voltage occurs at an r-f operating frequency considerably above that of the unloaded resonant frequency (approximately a 25-kHz shift). The corresponding changes in the plate voltage (d-c potential supply voltage as measured at the d-c power source --- see Fig. 2) and total d-c current (d-c current drawn from the power supply which principally includes the power amplifier plate current and the buffer-driver amplifier plate currents) are also shown in Fig. 12. The total d-c power input is related to the product of the plate voltage and the total d-c power amplifier plate current. The distinct drop-off in the plate voltage at both the highest and lowest operating frequencies shown in Fig. 12 indicates off-resonance operation. The increase in total d-c current occurring at the low operating frequencies is partly a result of the drooping electrical operating characteristic curve of the power supply. Apparently the high-frequency operating range was not sufficiently displaced off resonance to cause the same change in the total d-c current. Additional data from this test is discussed in a following section.

Energy Balance for Highest Power Operating Conditions

Figure 13 is a sketch of the radiant energy source configuration illustrating the power losses for the highest power operating point. This was also the test condition for maximum radiation through the inner transparent wall. The test conditions were: total discharge power, 223 kw; chamber pressure, 7.0 atm; argon weight flow rate, 0.033 lb/sec; and r-f operating frequency, 5.5873 mHz. These conditions resulted in the following power breakdown: 16.2 kw was radiated through the peripheral-wall water-dye coolant, 153.4 kw was deposited into the peripheral wall water-dye coolant, 49.5 kw was the total power deposited in both end walls, and 4.3 kw was convected out both thru-flow exhaust ports. The corresponding coolant flow rates and associated temperature rises are also indicated in Fig. 13. The discharge diameter at the axial midplane in this test was 0.75 in. The corresponding discharge

surface area and discharge volume were 3.9 sq. in. and 0.58 $in.^3$, respectively. The total d-c input power to the induction heater, Q_I, was 640 kw. This corresponds to an r-f system coupling efficiency (defined as the ratio of the total discharge power Q_T, to the total d-c input power Q_I) of 34.9 percent.

The maximum power condition (223 kw) was the highest reached prior to the onset of a flow instability discussed in the section entitled Results of Exploratory Tests Directed Toward Further Increases in Pressure and Power. As discussed there, further increases are possible after certain modifications are made.

Based on the estimates of conduction heat loss through the inner peripheral wall discussed previously, the total power radiated through the inner peripheral wall was calculated to be 162 kw. This resulted in a radiant energy flux Φ_R of 41.5 kw/sq in.; the corresponding equivalent black-body temperature was 10,420 R. The fraction of total discharge power radiated through the inner peripheral wall, $Q_{R,T}/Q_T$, was 0.72.

Due to the manner in which the end wall assemblies are designed (Fig. 13), it is not possible to obtain separate measurements of (1) the heat load on the end-wall face and (2) the power convected out of the test chamber through the thru-flow ports. As shown in Fig. 13, the end-wall assembly cooling water removes heat from both the end-wall face and the thru-flow exhaust duct (the duct between the thru-flow port and the thru-flow calorimeter). Accordingly, additional tests were conducted with one end wall modified as shown in Fig. 14. This sketch illustrates the separately cooled 0.80-in.-dia end-wall face cap that was employed. The face cap was fabricated from copper and was thermally isolated from the main, concentrically located, end wall. Independent water lines provided the necessary cooling water for the face cap. The face cap was highly polished using the same procedure used for the face of the regular end wall. To provide an indication of the local surface temperatures reached at various locations on the end wall and face cap, temperature-sensitive paints of various ranges were used in some tests (Fig. 14). To permit a direct comparison with earlier tests, the distance between the left end wall and the right end-wall face cap was maintained at 2 in. The main difference between this configuration and the radiant energy source configuration shown in Fig. 8(a) was that only the left injector manifold was used to drive the vortex (this resulted in a slight asymmetry in the shape of the discharge). To aid in simulating the configuration shown in Fig. 8(a) more closely, a copper shield was located at a position symmetric with the location of the left vortex injector manifold (see Fig. 15(b)).

Figure 15 shows the test configuration used and a typical test result. Approximately 90 percent of the total power deposited into the water-cooled copper end-wall assembly is due to conduction and convection from the hot gas being removed through the thru-flow ports and 10 percent is deposited directly into the end-wall face. For the power loss breakdown shown in Fig. 15(b), the total power deposited into

the discharge was approximately 34 kw. The separately cooled end-wall face cap absorbed 0.93 kw of power compared with 7.12 kw convected out the thru-flow port. A significant fraction of the total power deposited into the end-wall face cap is due to direct radiation from the radiant energy source. The temperature-sensitive paint confirmed the earlier belief that local temperatures on the exterior of the end-wall assembly away from the end-wall face were relatively low.

Factors Which Influence Source Radiation Characteristics

Total Discharge Power

Figure 16 shows the variation of discharge power per unit volume, Q_T/V, with total discharge power, Q_T. For reference, lines of constant discharge volume of 0.25 $in.^3$, 0.5 $in.^3$, and 1.0 $in.^3$ are also shown. The open symbols correspond to the data obtained from Ref. 15 using the configuration employing the earlier vortex injector manifold shown in Fig. 8(b). The solid symbols correspond to the most recent test results using the configuration employing the vortex injector manifold shown in Fig. 8(a). In general, the discharge power per unit volume increased as the total discharge power increased. The highest discharge power per unit volume of 0.57 megw/$in.^3$ occurred at a total discharge power of approximately 160 kw, an argon weight flow rate of 0.027 lb/sec, and a chamber pressure of 19.2 atm. This chamber pressure was the highest reached in any of the tests reported herein. The section entitled Results of Exploratory Tests Directed Toward Further Increases in Pressure and Power includes a discussion of changes required to obtain higher pressures.

A comparison can be made between the levels of discharge power per unit volume obtained in the present tests with those obtained in Refs. 15 and 23. The highest discharge power per unit volume obtained in the tests of Ref. 15 was 0.33 megw/$in.^3$. The present level of 0.57 megw/$in.^3$ represents approximately a 75-percent increase. In Ref. 23, the discharge power per unit volume was not given. However, it can be estimated, assuming a cylindrical discharge with a diameter and length equal to 75 percent of the 3.5-in. r-f torch diameter. This calculation gives 0.028 megw/$in.^3$ as the power per unit volume for the pure argon discharge.

Source Radiation Flux

For the data shown in Fig. 11 and tabulated in Table III, calculations of the approximate radiant energy flux, Φ_R, at the surface of the discharge were made. This flux was defined as the total radiated heat transferred through the inner fused silica tube (Fig. 10) (subject to the conduction correction discussed previously) divided by the surface area of the ellipsoidal discharge, i.e., $Q_{R,T}/A_S$. The flux defined in this way is approximately equal to the true radiant energy flux. Figure 17

shows this variation of radiant energy flux, Φ_R, with total discharge power, Q_T. Also included for comparison are the radiant energy fluxes achieved using the earlier vortex injector end-wall assembly reported in Ref. 15.

The highest level of radiant energy flux achieved was 49 kw/sq in. (the same condition as for maximum power density). Also, occurring at a chamber pressure of 19.2 atm and a total discharge power of approximately 160 kw. This corresponds to an equivalent black-body radiating temperature T^* (based on total heat flux and equivalent surface area) of about 10,860 R. The equivalent black-body radiating temperatures corresponding to the radiant energy fluxes for the test data are shown on the right side of Fig. 17. Recall that the heat flux in the reference nuclear light bulb engine design is about 178 kw/sq in.; this corresponds to an equivalent black-body temperature of 15,000 R. The heat flux in a derated nuclear light bulb engine design (Ref. 1) is about 14 kw/sq in.; this corresponds to an equivalent black-body temperature of 8000 R. As an additional reference point, the equivalent black-body radiating temperature of the sun is about 10,400 R. Thus, the maximum equivalent black-body radiating temperature achieved in the tests reported herein exceeds that of the sun, exceeds that of the derated engine, and is 72 percent of that of the reference engine.

R-F Operating Frequency

Figure 18 shows the effect of r-f operating frequency on the total discharge power and radiation characteristics for the corresponding range of test conditions illustrated in Fig. 12. The total discharge power, Q_T, shows a peak at approximately the loaded resonant frequency. The power radiated to the radiometer increased approximately 150 percent from 1.5 kw to 3.75 kw as the r-f operating frequency was increased from 5.5610 mHz to 5.6060 mHz. The distinct decrease in the discharge diameter at the low frequency range manifests itself in the curve of power density. Very high power densities are achieved just prior to reaching the frequency limit at which discharge extinguishment occurs. A similar, but less dramatic, effect is shown by the curve of radiant energy flux. This is due to the difference in slopes between the power radiated curve and the total discharge power curve at the lower r-f operating frequency range. Unfortunately, it was not possible to change the frequency during higher power tests because of the extreme sensitivity of the coupling parameters and the sensitivity limits of the instrumentation used. However, several other preliminary tests conducted at slightly higher power conditions than those in Fig. 18 indicate that the trend appears to be a shift of the approximate loaded resonant frequency towards lower frequencies (i.e., toward the unloaded resonant frequency). This may be part of the reason for the difficulty in achieving stable and steady discharges at the highest power and pressure conditions. Apparently low- and moderate-power discharges require a certain frequency range relative to the unloaded frequency for optimum operation from the stability standpoint, but as higher chamber pressures and total discharge powers are reached, the system must be

continuously retuned to provide maximum discharge stability and improved r-f coupling. It appears that future increases in radiant energy flux may be obtained by gradually shifting the r-f operating frequency to compensate for the changing electrical characteristics of the plasma as transition into the higher power and pressure regime is reached.

Caution must be exercised in comparing the results obtained at these relatively low power, pressure and flow rates with results of higher level test conditions. The results obtained are valuable, however, to qualitatively help explain many of the trends which may occur.

Test Chamber Pressure

The effects of chamber pressure on radiated power efficiency, $Q_{R,T}/Q_T$ (the fraction of total discharge power that was radiated through the inner transparent wall), are shown in Fig. 19. The figure shows this trend for total discharge power levels between about 60 and 160 kw. As expected, increases in chamber pressure resulted in increases in the fraction of discharge power that was radiated. The maximum pressure of any test conducted during this program was 19.2 atm. For the data shown, the values of $Q_{R,T}/Q_T$ ranged from about 0.55 at 3 atm to about 0.85 at 19.2 atm. Note that the maximum pressure data point did not correspond to the maximum value of fraction of total discharge power that was radiated. This may have occurred because the r-f operating frequency corresponding to the maximum pressure point was reduced approximately 8 kHz below the frequency corresponding to the somewhat lower operating pressure of 17.5 atm. However, it is evident that increasing pressure allows operation of the r-f plasma in a highly radiation-dominated mode.

Temperature Distribution

To obtain an estimate of the radial temperature distributions within the r-f plasma discharge at the axial midplane for different test conditions, a series of spectral emission measurements were made. The monochromator system was aligned so that it viewed across a diameter of the discharge at the axial midplane. The absolute value of the plasma continuum radiation was measured along a diameter of the plasma at a wavelength of 4320 Å. By assuming thermodynamic equilibrium, the temperature of the plasma was determined from the continuum radiation measurements using the method described in Ref. 10 for relating the continuum intensity to the temperature. A machine program employing the Abel inversion method was used to convert the measured chordal intensities to radial intensities. A complete detailed description of the data reduction techniques is presented in an appendix in Ref. 10.

Figure 20 shows six typical radial distributions of temperature that were obtained for the various test conditions noted. To investigate the effect of chamber pressure on shifting the temperature profiles, the pressure was increased by a factor of 8 (from 1 to 8 atm). Similarly, the total discharge power was varied by a factor of about 5 (from 25 to 120 kw). The r-f operating frequency and the argon flow rates were adjusted for each case to maintain approximately constant discharge diameters of about 0.8 in. (see lower right-hand corner of Fig. 20).

As expected, the distributions in Fig. 20 exhibit a distinct off-axis peak. This is primarily due to the mechanism of depositing r-f power into an annular region. In all cases, the off-axis peak occurred at approximately the mid-radius of the discharge. This is in good agreement with the results of Refs. 10, 15 and 25. The peak temperatures obtained over the range of test conditions shown varied between 21,700 and 22,850 R, with the lowest peak temperature corresponding to the low-power, low-pressure case and the highest temperature corresponding to the high-power case at 6 atm (the peak temperature at 8 atm was very slightly lower). The corresponding centerline temperatures were approximately 1000 to 1500 R lower than the peaks.

It is interesting to note from the radial profiles of temperature shown (occurring over a fairly wide range of discharge powers and pressures) that relatively small differences in profile shape, and only about 5-percent differences in peak temperature, occurred between the various cases. For reference, the range of the intensity-averaged temperatures for the six cases is also shown (calculated from the integrated average intensity using the relationships between intensity, temperature, and radius).

The relatively small change in discharge temperature (both centerline and peak) over the fairly wide range of discharge powers and pressures in these data make it interesting to compare the results with those obtained from theoretical consideration. The curves in Fig. 21 show the calculated variation of radiated power per unit volume for an argon plasma versus temperature with pressure as a parameter. The procedure outlined in Ref. 21 was used to calculate these curves. The power radiated per unit volume includes contributions due to both line and continuum radiation between 0.3 and 1.0 microns. The experimental data corresponding to the six test conditions shown in Fig. 20 are illustrated by the open symbols in Fig. 21. In plotting the data, the points were located on the theoretical curves (pressure corresponding to pressure in the tests) at the total radiated power per unit volume determined from $Q_{R,T}/V$ in the tests. The temperatures determined from the data in this manner ranged between 21,600 and 22,400 R for the six test conditions of Fig. 20, compared with peak temperatures from spectroscopic measurements between 21,700 and 22,850 R. Also included for reference (shown by the solid symbols) are the experimental data corresponding to the highest chamber pressure (19.2 atm) and the highest total discharge power (223 kw) test conditions.

The results appear to indicate that varying total discharge power and chamber pressure do not significantly change the temperature of the vortex stabilized r-f argon plasma for the range of test conditions and for the configuration investigated. Seed material (Ref. 9), in either particle or gaseous form, can be used to shift the emission spectrum towards the ultraviolet (Ref. 18). For a given discharge volume and total discharge power, this shift can result in a significant decrease in plasma temperature. This shift is desirable in future tests using the radiant energy source to simulate more closely both the flux level and the spectrum anticipated in the reference nuclear light bulb engine.

Spectral Distribution of Radiant Energy

To obtain an estimate of the power radiated through the peripheral-wall coolant (with and without dye added) in various wavelength bands, a series of tests was conducted at different discharge power and pressure levels. Typical test results are presented in Fig. 22. A sketch of the configuration is also shown. The test conditions are shown in the left-hand column of the table. The first case shown is for a discharge at 3 atm with an argon weight flow rate of 0.028 lb/sec and a total discharge power of 55 kw. No dye was added to the peripheral-wall coolant. The approximate spectral distribution of the power radiated through the peripheral-wall coolant (measured using the radiometer system) in the four wavelength bands are shown in the table in kw and (in parentheses) as a percentage of Q_R. At the first test condition, approximately 75 percent of the total power radiated through the peripheral-wall coolant is in the wavelength band from 0.72-to-1.3 microns (for this case the equivalent T^* is about 7400 R). For reference, approximately 85 percent of the radiation from a black-body at 15,000 R is between 0.25 and 1.3 microns. Without changing any of the test conditions, 800 ppm of nigrosine dye was added to the annular cooling water (second case in Fig. 22). Again, a significant portion of the total radiated power appears in the 0.72-to-1.3 micron wavelength band. Note that the dye concentration was sufficient to reduce the total radiation from the source by a factor of approximately four (as expected based on the data in Fig. 7). It was expected that as higher discharge powers and chamber pressures were reached, a greater percentage of the radiated power would shift to lower wavelengths. The third case in Fig. 22 illustrates this trend. In this case, the total discharge power was increased above the previous case by approximately a factor of two (from 55 to 117 kw) and the chamber pressure was raised from 3 to 5 atm. The dye concentration was maintained at 800 ppm. The results indicate a slight increase in the percent of power radiated in the lower wavelength bands, particularly between 0.25 and 0.3 microns. This trend is also in agreement when compared with the approximate trends of percent of total radiation that should be present assuming the plasma radiates like a black-body at the temperatures calculated for both cases from $Q_{R,T}/A_S$. In the first case (with dye) the equivalent black-body temperature is about 7400 R. The approximate percentage breakdown for the 0.25-0.3, 0.3-0.72,

0.72-1.0 and 1.0-1.3 micron wavelength band is 1, 39, 36 and 25 percent, respectively. For the second case, the equivalent black-body radiating temperature based on total heat flux is about 8750 R. The percent breakdown of the total radiation in each of the same wavelength bands as above is 1, 49, 31.5 and 18 percent, respectively. This comparison also indicates the future requirement for seeding the plasma in order to shift its spectrum closer to that of a black-body. For comparison, APPENDIX B describes spectral emission measurements over the wavelength range 0.15 to 0.43 microns made with direct viewing of the plasma discharge (through no fused silica tubes or annulus of cooling water).

Comparison of Source Characteristics with those Desired in Reference Engine

Based on the test results reported herein and available information on the reference engine and early in-reactor type test conditions, a comparison can be made between various important parameters. Table IV includes details related to the transparent wall configuration, significant length and diameter dimensions, the coolant and buffer fluids used, corresponding gas weight flow rates, chamber pressures, and the heat deposition rates and heat fluxes. The full-scale engine data shown was obtained from Ref. 1, the early in-reactor test configuration* data from Ref. 11, and the r-f plasma radiant energy source data from the tests reported herein. The r-f plasma source was assumed to be ellipsoidal in shape for calculating the radiant heat flux per unit area; the transparent wall configuration surrounding the plasma source was taken to be 3 in. long in the calculations of total heat flux deposited into the wall.

The comparison illustrates that in the present state of development, the r-f plasma radiant energy source can provide equivalent black-body radiating temperatures about 35 percent above those required for simulating the full-scale derated engine heat flux and 55 percent above those required for simulating an early in-reactor test configuration heat flux. The full-scale reference engine and early in-reactor tests require chamber pressures of about 500 atm. The highest chamber pressures used in radiant energy source tests was about 20 atm. To permit significant increases in chamber pressure, initial tests of filament-wound pressure vessels for possible future use in the radiant energy source research program were conducted (refer to Appendix A).

*Several in-reactor test configurations are under study. The one cited here would be for the Pewee reactor and would have a flux of 8.36 kw/sq in. ($T^* = 7040$ R).

A graphical comparison between experimental test results from the 1.2-megw r-f radiant energy source and radiation flux levels desired for simulating the full-scale engine or an early in-reactor test configuration, including additional details of the r-f plasma radiant energy source, is shown in Fig. 23. The plot shows the variation of total radiation, $Q_{R,T}$, from the source with discharge diameter. The source was assumed to be ellipsoidal with a major axis of 2 in. For reference, dashed lines of constant radiant energy flux corresponding to the full-scale reference and derated engines and an early in-reactor test configuration are shown. Also shown are the corresponding equivalent black-body radiating temperatures, T^*. The cross-hatched area on the figure indicates the envelope of experimental test results obtained from Ref. 15. The solid symbols correspond to the most recent test results. The maximum radiation heat flux of 49 kw/sq in. corresponds to a total radiation from the source of 131 kw (equivalent black-body radiating temperature of 10,860 R).

Simultaneous simulation of both the radiant energy flux and pressures of the full-scale nuclear light bulb engine and/or an early in-reactor test configuration require r-f plasma test equipment capable of operating at significantly higher pressures. With this in mind, work was initiated on the use of filament-wound pressure vessels. Thin-walled vessels were hydrostatically tested to pressures above 500 atm and were operated within r-f field environments. These results are discussed in Appendix A.

Results of Exploratory Tests Directed Toward Further Increases in Pressure and Power

A series of tests were conducted to investigate factors and test conditions that may have an influence on discharge behavior and stability. In particular, exploratory tests were directed at trying to determine the factors that have imposed the present operating limitations (chamber pressure (19.2 atm) and total discharge power (223 kw)). In general, the instabilities observed to occur can be categorized into two types; the first is apparently associated with gas breakdown phenomena; the second is associated more with the flow conditions (i.e., vortex injection velocity, vortex flow pattern and associated secondary flows and unbalance of the thru-flow port argon flow rates). These possible sources of discharge instability undoubtedly are coupled. However, in particular operating regimes and under certain test conditions, one or the other appears to dominate.

The first type occurred in the high-pressure operating regime, particularly when the resonator voltage exceeded a certain level corresponding to that particular operating pressure. This usually occurred at operating frequencies less than the unloaded resonant frequency. The goal of trying to maintain as small a discharge as possible (with its associated high radiant flux) necessitated increasing the

argon weight flow and pressure. As a result, the resonator voltage increased significantly (see Table III). When the instability occurred, the discharge jumped out of the test section between the end walls and became located around the periphery of one of the end walls (midway between the end-wall face and the vortex injector manifold). This breakdown-type of instability may have been aided by partial r-f heating of the stainless steel vortex injectors used (see Fig. 8(a)). To determine the level of r-f heating, a test was conducted in which the r-f system was operated at moderately high power conditions with no plasma discharge present. The stainless steel injectors and copper manifold were instrumented so that a calorimetric measurement could be made to determine the amount of r-f power deposited into the vortex injectors. The test results indicated that, at about 7-kv resonator voltage, approximately 0.12 kw of r-f power was deposited into the vortex injectors due to eddy current heating. The presence of these partially heated injectors in a recirculation zone associated with the particular type of flow pattern and geometry shown in Fig. 8(a) may have aided in initiating a breakdown and the instability phenomenon observed. The occurrence of this type of instability was difficult to predict; very little warning was given in the form of visual or electrical variations in the recording instruments. Frame-by-frame study of high-speed color movies provided additional information concerning this discharge relative instability, but the exact cause is still not understood.

The second type of instability observed to occur and believed related to the flow conditions was similar to that reported in Ref. 15 and usually occurred at operating frequencies greater than the unloaded resonant frequency. This type of flow instability limited the maximum discharge power to 223 kw as discussed in section entitled Energy Balance for Highest Power Operating Conditions. When the discharge was operated at test conditions other than those which provided a steady and stable discharge, random axial oscillations ($< 10^3$ Hz) occurred in the vicinity of the end-wall faces. Superimposed on these oscillations were radial pulsations, primarily attributed to the inherent 360 Hz ripple of the three-phase power supply. The random axial oscillations manifested themselves as small plasma flames which would partially extend over one of the end walls. This asymmetry in the axial direction indicated that possibly the amount of flow removed through each end-wall thru-flow port (flow balance) was a critical parameter in determining the stability of the discharge, particularly at high-power and high-pressure operating conditions. The test series conducted with the separately water-cooled end-wall face cap (see Fig. 14) also exhibited some asymmetry in the discharge. Recall, vortex injection in the latter test was from one end-wall assembly only.

To determine the possible effect of thru-flow port flow rate unbalance on discharge stability, tests were conducted using the configuration shown in Fig. 8(a). Thermocouples were located immediately downstream of the thru-flow exhaust ports in each end wall. Coarse and fine flow control valves, rotameters and exhaust gas

calorimeters were located downstream of the thermocouples. Tests were conducted in which the amount of flow removed through each end-wall thru-flow port was purposely unbalanced by fixed amounts. The results indicated similar behavior in the discharge as observed in the high-power, high-pressure tests where plasma flames were observed to fluctuate from one end of the discharge. The discharge became distorted in shape; it was larger near the end wall where the amount of flow through the thru-flow port was lower. At relatively high-power test conditions, the effect of this unbalance on discharge stability became more critical. The inside diameter of the thru-flow ports (0.185 in.) and valves and exhaust connections downstream may also have an effect on the thru-flow port flow-rate unbalance at the higher pressures and discharge powers.

Using the test conditions corresponding to the highest discharge power case (Q_T = 223 kw), estimations indicate that the flow through the thru-flow ports was close to the choked flow condition. Not knowing the temperature at the thru-flow port entrance or the effect of the swirl flow on choked flow conditions precludes an exact calculation from being made. The left and right end-wall exhaust systems (tubing length, bend locations, and intermediate heat exchangers) are not exactly identical and therefore it is possible that, as one or both of the thru-flow ports in the test chamber approach choked conditions, the amount of flow that can be removed through the thru-flow ports may not be enough to provide sufficient control of the discharge. Attempts to simultaneously adjust the flow control valves in the thru-flow port exit lines proved difficult; the discharge stability was sensitive to slight changes in the valve position.

To alleviate this possible restriction, future operation at higher total discharge power levels will require increasing the diameter of both thru-flow ports and using flow control valves with finer adjustment and minimum flow restriction.

The instability noted for the case when the chamber pressure was increased above 19.2 atm was not a result of possible choked-flow conditions in the thru-flow ports. The argon flow rate corresponding to the highest chamber pressure test was less than half the maximum isentropic argon weight flow possible based on choked-flow conditions.

The effect of vortex injection velocity on the stability and behavior of the discharge was investigated by operating the configuration shown in Fig. 8(a) with only the outer set of 8 vortex injectors on each end wall providing the argon flow to the test chamber. Under approximately the same test conditions, changing from a total of 32 to 16 vortex injectors results in a factor-of-two increase in vortex injection velocity. Decreases of approximately 5 percent in power radiated and resonator voltage were measured. By changing from the outer set of 8 vortex injectors on each end wall to only the inner set of 8, increases of approximately 5 percent in Q_R and V_R over the case using all 16 vortex injectors on each end wall resulted.

No discharge diameter scans were made during this series of tests. These results seem to indicate that changes in vortex injection velocity may not be of principal importance in determining discharge stability within the operating regime of the tests reported herein. Effects not investigated, but which may have a direct influence on discharge stability, are the axial component introduced in the flow at the vortex injector tips (see Fig. 9) and the end wall diameter. A change in the axial component and the end wall diameter may be required in future tests in the higher pressure regime.

The shift in the impedance of the discharge as higher chamber pressures and total discharge powers are reached is another possible origin for initiating discharge instability. The results of several exploratory tests conducted at discharge powers and chamber pressures greater than those shown in Fig. 12 indicated the following trend: the loaded resonant frequency shifts toward lower values (i.e., toward the unloaded resonant frequency) as higher power and pressure conditions are reached. Future modification may be necessary to increase the sensitivity of the r-f tuning circuit which will permit continuous r-f operating frequency adjustment as the chamber pressure and total discharge power are increased.

REFERENCES

1. McLafferty, G. H. and H. E. Bauer: Studies of Specific Nuclear Light Bulb and Open-Cycle Vortex-Stabilized Gaseous Nuclear Rocket Engines. United Aircraft Research Laboratories Report F-910093-37, prepared under Contract NASw-847, September 1967. Also issued as NASA CR-1030, 1968.

2. Clark, J. W., B. V. Johnson, J. S. Kendall, A. E. Mensing, and A. Travers: Summary of Gaseous Nuclear Rocket Fluid Mechanics Research Conducted Under Contract NASw-847. United Aircraft Research Laboratories Report F-910091-13, May 1967.

3. McLafferty, G. H.: Investigation of Gaseous Nuclear Rocket Technology --- Summary Technical Report. United Aircraft Research Laboratories Report H-910093-46, prepared under Contract NASw-847, November 1969.

4. McLafferty, G. H.: Survey of Advanced Concepts in Nuclear Propulsion. Journal of Spacecraft and Rockets, Vol. 5, No. 10, October 1968.

5. McLafferty, G. H.: Absorption of Thermal Radiation in the Transparent Wall of a Nuclear Light Bulb Rocket Engine. Journal of Spacecraft and Rockets, Vol. 4, No. 6, June 1967.

6. Travers, A.: Experimental Investigation of Radial-Inflow Vortexes in Jet-Injection and Rotating-Peripheral-Wall Water Vortex Tubes. United Aircraft Research Laboratories Report F-910091-14, prepared under Contract NASw-847, September 1967. Also issued as NASA CR-1028, 1968.

7. Vogt, P. G.: Development and Tests of Small Fused Silica Models of Transparent Walls for the Nuclear Light Bulb Engine. United Aircraft Research Laboratories Report J-910900-3, prepared under Contract SNPC-70, September 1970.

8. McLafferty, G. H.: Gas Core Nuclear Rocket Engine Technology Status. AIAA Paper No. 70-708, presented at the Sixth AIAA Propulsion Joint Specialist Conference held in San Diego, California, June 11, 1970.

9. Klein, J. F. and W. C. Roman: Results of Experiments to Simulate Radiant Heating of Propellant in a Nuclear Light Bulb Engine Using a D-C Arc Radiant Energy Source. United Aircraft Research Laboratories Report J-910900-1, prepared under Contract SNPC-70, September 1970.

REFERENCES (Continued)

10. Jaminet, J. F. and A. E. Mensing: Experimental Investigations of Simulated Fuel Containment in R-F Heated and Unheated Two-Component Vortexes. United Aircraft Research Laboratories Report J-910900-2, prepared under Contract SNPC-70, September 1970.

11. Latham, T. S. and H. E. Bauer: Analytical Studies of In-Reactor Tests of a Nuclear Light Bulb Unit Cell. United Aircraft Research Laboratories Report J-910900-6, prepared under Contract SNPC-70, September 1970.

12. Bauer, H. E., R. J. Rodgers, and T. S. Latham: Analytical Studies of Start-Up and Dynamic Response Characteristics of the Nuclear Light Bulb Engine. United Aircraft Research Laboratories Report J-910900-5, prepared under Contract SNPC-70, September 1970.

13. Palma, G. E. and R. M. Gagosz: Optical Absorption in Transparent Materials During 1.5 Mev Electron Irradiation. United Aircraft Research Laboratories Report J-910929-1, prepared under Contract SNPC-70, September 1970.

14. Krascella, N. L.: Analytical Study of the Spectral Radiant Flux Emitted from the Fuel Region of a Nuclear Light Bulb Engine. United Aircraft Research Laboratories Report J-910904-1, prepared under contract SNPC-70, September 1970.

15. Roman, W. C., J. F. Klein, and P. G. Vogt: Experimental Investigations to Simulate the Thermal Environment, Transparent Walls and Propellant Heating in a Nuclear Light Bulb Engine. United Aircraft Research Laboratories Report H-910091-19, prepared under Contract NASw-847, September 1969.

16. International Critical Tables, Vol. V. McGraw-Hill Book Co., Inc., New York, 1930.

17. Lukens, R., private communication. Fisher Scientific Corporation, Springfield, New Jersey, September 1970.

18. Marteney, P. J., A. E. Mensing, and N. L. Krascella: Experimental Investigation of the Spectral Emission Characteristics of Argon-Tungsten and Argon-Uranium Induction Heated Plasmas. United Aircraft Research Laboratories Report G910092-11, prepared under Contract NASw-847, September 1968. Also issued as NASA CR-1314.

19. Olsen, H. N.: Measurements of Argon Transition Probabilities using the Thermal Arc Plasma as a Radiation Source. Journal of Qualitative Spectroscopy and Radiative Transfer, Vol. 3, 1963, pp. 59-76.

REFERENCES (Continued)

20. Mensing, A. E. and J. S. Kendall: Experimental Investigation of Containment of a Heavy Gas in a Jet-Driven Light-Gas Vortex. United Aircraft Research Laboratories Report D-910091-4, prepared under Contract NASw-847, March 1965.

21. Mensing, A. E. and L. R. Boedeker: Theoretical Investigation of R-F Induction Heated Plasmas. United Aircraft Research Laboratories Report G-910091-18, prepared under Contract NASw-847, September 1968. Also issued as NASA CR-1312.

22. Soshnikov, V. N. and E. S. Trekhov: The Theory of High-Frequency Vortex Discharges at High Temperature, I. High Temperature, Vol. 4, No. 2, March-April 1966, pp. 165-171.

23. Thorpe, M. L.: Radio-Frequency Plasma Simulation of Gas-Core Reactor. Journal of Spacecraft and Rockets, Vol. 6, No. 8, August 1969.

24. Griem, H. R.: Plasma Spectroscopy. McGraw-Hill Book Co., Inc., New York, 1964.

25. Mensing, A. E. and J. F. Jaminet: Experimental Investigation of Heavy-Gas Containment in R-F Heated and Unheated Two-Component Vortexes. United Aircraft Research Laboratories Report H-910091-20, prepared under Contract NASw-847, September 1969.

26. Krascella, N. L.: Theoretical Investigation of the Composition and Line Emission Characteristics of Argon-Tungsten and Argon-Uranium Plasmas. United Aircraft Research Laboratories Report G-910092-10, prepared under Contract NASw-847, September 1968.

LIST OF SYMBOLS

A_S	Discharge surface area, sq in.
C	Dye concentration, ppm
d	Discharge diameter, in.
f	Frequency, mHz or kHz
I_L	Total intensity of the continuum, w/cm^2-micron
I_P	Total d-c current, amp
I_λ	Monochromatic intensity, kw/cm^2-ster
$I_{o,\lambda}$	Incident monochromatic intensity, kw/cm^2-ster
$I_\lambda/I_{o,\lambda}$	Internal transmittance, dimensionless
$I_{\Delta\lambda}/I_{o,\Delta\lambda}$	Dye transmittance in 0.25-1.3 micron wavelength band, dimensionless
L	Length of unit cavity or transparent wall model, in. or ft
P	Total pressure, atm or psia
P_D	Chamber pressure, atm
Q_C	Power conducted through inner peripheral wall, kw
Q_E	Power deposited in end-wall cooling water, kw
Q_I	Total d-c input power to r-f induction heater, kw
Q_L	Power convected through thru-flow exhaust ports, kw
Q_R	Radiated power escaping test chamber as measured by radiometer, kw
Q_T	Total discharge power, $Q_R + Q_W + Q_E + Q_L$, kw
Q_W	Power deposited in peripheral wall coolant, kw

LIST OF SYMBOLS (Continued)

$Q_{R,T}$	Total radiated power through inner peripheral wall, $Q_R + Q_W - Q_C$, kw
$Re_{t,j}$	Injection Reynolds number based on average inlet jet velocity, dimensionless
r	Local radius from center of chamber or discharge radius, in. or ft
T	Temperature, deg R or deg K
T_{AV}	Intensity-averaged temperature in plasma, deg R or deg K
T^*	Equivalent black-body radiating temperature, deg R
t	Time, sec
V	Discharge volume, $in.^3$
v	Local velocity, ft/sec
v_l	Tangential velocity at periphery, ft/sec
v_j	Average buffer-gas injection velocity, ft/sec
V_P	Plate voltage, kv
V_R	Resonator voltage (zero-to-peak), kv
W	Filament-wound tube weight, lb
W_A	Argon weight flow rate, lb/sec
W_C	Coolant weight flow rate, lb/sec or gpm
Z_t	Filament-wound tube weight parameter, $lb/atm\text{-}ft^3$
α	Coefficient of thermal expansion, cm/cm/deg C
η	R-F system coupling efficiency, Q_T/Q_I, dimensionless
Φ_R	Radiant energy flux from surface of the plasma, $Q_{R,T}/A_S$, $kw/in.^2$
λ	Wavelength, microns or Å

APPENDIX A

SUPPORTING RESEARCH ON FILAMENT-WOUND TUBES*

This appendix describes development and initial tests of filament-wound pressure vessels for application to future high-pressure r-f light source tests. Future tests using the 1.2-megw r-f induction heater and early in-reactor "proof of principle" tests may require that pressures up to 500 atm be employed. At these pressures, standard fused silica tubing as used in the tests described in the main text is not practical as a pressure vessel. However, fiberglass filament-wound tubes could be utilized at these pressures, provided they are compatible with the r-f radiant energy source environment.

Initially, a filament-wound tube suitable for low-pressure service with end closures was obtained from United Technology Center (Division of United Aircraft Corporation) and was hydrostatically tested. The approximate tube dimensions were: length = 12 in., diameter = 4 in., and wall thickness = 0.030 in. (including resin). During these hydrostatic tests some seepage through the windings occurred. This seepage was eliminated by coating the inside surface of the tube with a silicon-rubber sealant. In future tests, some method of sealing filament-wound pressure vessels must be utilized to prevent seepage through the windings at pressures greater than about 6 atm.

Two specimen tubes were fabricated at the United Aircraft Research Laboratories. One tube consisted of nine layers of fiberglass roving (six layers in the hoop direction and three layers in the longitudinal direction) with a wall thickness of approximately 0.060 in. This tube was positioned around the outer quartz tube in the 80-kw r-f induction heater (see Ref. 10 for a detailed description of this test facility). In tests with only r-f fields present, no measurable r-f power was deposited in the tube.

The second filament-wound tube consisted of twelve layers of fiberglass roving (eight layers in the hoop direction and four layers in the longitudinal direction). The wall thickness was approximately 0.11 in. and the length was approximately 6 in. This tube was also installed in the 80-kw heater (see Figs. 24(a) and (b)), in place of the outer fused silica tube normally used (see Ref. 10). Nigrosine dye was added to the cooling water in the annulus formed by the inner (fused silica) and outer (filament-wound) tubes in order to absorb the radiation from the plasma. The radiation escaping could overheat and damage the filament-wound tube. It was determined

*Tests conducted by Jerome F. Jaminet.

that no inner sealing liner was necessary as the filament-wound tube did not leak cooling water at line pressure (up to about 40 psig). Figure 24(c) is a photograph of the tube during operation with an r-f plasma. The plasma appears to fill the tube due to diffusion of the light passing through the tube wall. The plasma was about 1-in. in dia (the tube has a 2.0-in.-ID).

Calibration of the radiant energy attenuation by a filament-wound pressure shell used in high-pressure r-f plasma tests would be a requirement. To determine a representative value, this second tube was also tested for light attenuation using a tungsten filament standard lamp. Results indicated that approximately 1 percent of the incident light throughout the spectrum from 0.3 to 0.9 microns was transmitted through one wall of the tube.

A hydrostatic-test fixture was fabricated to stress this tube in the circumferential direction. The tube was subjected to an internal pressure of 8000 psig (530 atm). (Testing was stopped at this pressure due to failure of the test fixture used to hold the tube.) After this test, the inside of the filament-wound tube had numerous small axially-oriented surface cracks, indicating that the strain limit of the bonding resin had been exceeded. At 8000 psig internal pressure, the hoop stress on the tube is approximately 110,000 psi --- well below the theoretical ultimate stress of 200,000 psi.

A tube weight parameter, $Z_t = W/PV$, where W = tube weight in lb, P = internal pressure in atm, and V = test volume in ft^3, was calculated for the tube utilized in the above tests. For a pressure of 530 atm, $Z_t = 0.0584$ lb/atm-ft^3, which compares reasonably well with the calculated pressure shell weight parameter given in Ref. 1 for the reference nuclear light bulb engine, $Z_t = 0.0695$ lb/atm-ft^3. The difference in the two weight parameters may be partially accounted for by the differences in shape of the two pressure vessels and by the absence of ends on the tube.

The epoxy resin used to fabricate the above filament-wound tubes was Union Carbide ERL-2256. This laminating resin has an r-f dissipation factor of approximately 0.025. The dissipation factor of a material is a measure of the energy that is lost in an r-f field by eddy current heating of the material. For comparison, the dissipation factor of fused silica is 0.0001. If problems caused by material heating in an r-f field are encountered in future tests, other epoxy resins are commercially available with dissipation factors as low as approximately 0.0025, as well as providing high strength at higher operating temperatures (on the order of 500 F).

The tests described above have demonstrated the feasibility of using filament-wound pressure vessels in future high-pressure tests involving r-f plasmas. Also, they have provided further confidence in the design of the filament-wound pressure shell for the full-scale reference nuclear light bulb engine design.

APPENDIX B

RESULTS OF SPECTRAL EMISSION MEASUREMENTS*

To provide additional information on the ultraviolet (u-v) portion of the spectrum of an argon plasma, an experiment was conducted using the UARL 1.2-megw r-f induction heater in which the plasma radiation was measured with no fused silica or annulus of water coolant in the radiation path. The equipment used for these tests is shown schematically in Fig. 25. Holes were blown in both the inner and outer fused silica tubes and a 0.315-in.-ID by 0.394-in.-OD fused silica tube was fused perpendicular to both the inner and outer fused-silica tubes (see Fig. 25). The small fused silica tube was joined to a copper tube that passed through the test tank to the monochromator entrance slit. Two 0.125-in.-dia apertures were located in the copper tube to collimate the light. A lithium fluoride window was secured to one end of the copper tube. (The u-v cutoff of lithium fluoride is about 0.115 microns.)

The Jarrel-Ash 0.25-meter monochromator (described in Ref. 15) was used in these tests. The entrance and exit slits of the monochromator were 100-microns wide. These slits were the smallest available that were open (i.e., not etched on a fused-silica back). The photomultiplier tube was an EMI 9558 with the face coated with sodium salicylate. Although the photomultiplier tube face is glass, the presence of the coating permits its use into the ultraviolet region. Sodium salicylate fluoresces under ultraviolet light and emits photons at a wavelength of approximately 0.41 microns. The quantum efficiency of the coated photomultiplier tube was assumed to be constant below approximately 0.35 microns.

This monochromator was not designed for use in the vacuum ultraviolet below 0.18 microns since it cannot be evacuated. Thus, for the tests discussed herein, the monochromator was purged with argon to permit radiation between 0.12 to 0.18 microns to pass through the system without being absorbed by oxygen. In setting up these experiments, it was determined that with this monochromator some higher wavelength light reaches the exit slit when the grating is set for the ultraviolet portion of the spectrum. Some of this higher wavelength light is always present in a double pass monochromator of this type, the remainder is believed to be scattered light from the grating. Because of the presence of this light, absolute intensity measurements of the ultraviolet emission could not be made. Instead, the radiation from the plasma was recorded twice: once with a pyrex plate (assumed to be opaque to u-v radiation) covering the entrance slit of the monochromator and once with no

*Tests conducted by Arthur E. Mensing.

covering. The difference in recorded intensity at a given wavelength was then assumed to be the true radiation. (Corrections were also made for the reflections from the pyrex plate.) The optical system shown in Fig. 25 was calibrated with a tungsten filament standard lamp, and against a plasma of known radiation (that used to determine the temperature profiles for case IV presented in Discussion of Results Section of this report).

Tests were conducted at four different chamber pressures and total discharge power levels of the argon plasma. The test conditions are listed in the table in Fig. 26. For each test the emitted spectrum between about 0.15 and 0.43 microns was recorded with and without the pyrex plate. The variation of emitted surface intensity, $I_L(w/cm^2-\mu)$ with wavelength is shown in Fig. 26. Very little radiation was detected below wavelengths of approximately 0.18 microns. This was expected since the only appreciable radiation would be continuum (there are no strong catalogued lines in this region of the spectrum) (also see Ref. 26). It was not possible with the instrumentation used to accurately detect radiation levels below approximately 2 $w/cm^2-\mu$.

A comparison was made between the power radiated in the wavelength band from 0.25 to 0.30 microns for the data of Case III in Fig. 22 with the value obtained from integrating the data from Case IV in Fig. 26 over the same wavelength band. The following assumptions were made: (1) the plasma discharge radiates uniformly over its surface area, (2) the BaF_2 window has a 0.25 μ nominal cut-off wavelength, and (3) no significant radiation absorption by the water in the 0.25 to 0.30 micron wavelength band occurred. For the test conditions of Case III (Fig. 22), 2.6 kw was radiated between 0.25 and 0.30 microns; while for the test conditions of Case IV (Fig. 26), 1.6 kw was radiated. The test conditions for these cases are not exactly identical and therefore, exact agreement is not expected.

TABLE I

SUMMARY OF SPECIFIC PROPERTIES OF FUSED SILICA TUBES
USED IN 1.2-MEGW R-F PLASMA RADIANT ENERGY SOURCE TESTS
(Property Data Obtained from Ref. 7)

Manufacturer	General Electric	
Type	204	
Impurities	76 ppm (average)	
Size of Inner Peripheral Wall	2.24-in.-ID x 2.38-in.-OD	
Size of Outer Peripheral Wall	2.54-in.-ID x 2.88-in.-OD	
Measured Wall Thickness Variation		
Inner Wall	±20 Percent	
Outer Wall	±30 Percent	
Service Temperatures		
Normal	900 C	
Extreme	1100 C	
Annealing Point	1070 C	
Softening Point	1670 C Approximately	
Melting Point	1800 C Approximately	
Coefficient of Thermal Expansion	α x 10^{-6} cm/cm/C 0-300 C α = 0.55	
Density	2.22 g/cm^3	
Specific Heat	0.25 cal/g-C at 500 C	
Thermal Conductivity	0.011 cal/cm-g-C at 800 C	
U-V Cut-Off at 50% Transmission	0.21 μ	For 0.4-in. Thickness, Excluding Surface Reflection Loss
I-R Cut-Off at 50% Transmission	3.6 μ	
Range of Tensile Strength for Tubes Tested		
2.24-in.-ID x 2.38-in.-OD	3600-4100 psi	Indicated Hoop Stress at Failure
2.54-in.-ID x 2.88-in.-OD	4000-4500 psi	

TABLE II

TYPICAL OPERATING PROCEDURE FOR THE 1.2-MEGW
R-F INDUCTION HEATER

1. 1.2-megw r-f induction heater system was turned on.

2. All diagnostic and recording equipment was turned on and zero-reference calibrated.

3. All cooling water and argon gas systems were turned on and set to the desired starting conditions.

4. The auxiliary d-c starter system was turned on and both electrodes were indexed into contact position.

5. The r-f drive system was tuned for the proper resonant frequency.

6. The d-c voltage supplied to the power amplifiers was increased to 3.5 kv by varying the saturable reactor control (see Figs. 2 and 4).

7. The d-c starter system was activated at the 3.5-kv point; plasma was established.

8. The starter electrode assemblies were removed from the end-wall thru-flow ports.

9. The end-wall thru-flow starter electrode ports were plugged to route all argon exhaust gas through both exhaust gas flow control and calorimeter systems.

10. The d-c supply voltage to the power amplifiers was increased to 5 kv and was accompanied by a corresponding increase in argon weight flow rate.

11. The r-f drive system was then retuned to compensate for the resonant frequency change due to the presence of the r-f plasma discharge within the r-f work coils and/or to provide the desired degree of stability required for a particular operating test condition.

12. Known concentrations of nigrosine dye were added to the annular cooling water reservoir tank to maintain the radiation escaping the test chamber at safe levels.

13. The r-f input power, argon weight flow rate to the vortex injector system and chamber pressure were increased to the level desired for a particular test condition.

TABLE II (Continued)

14. All required measurements and data acquisition were taken at a particular test condition (average run time of the 1.2-megw r-f induction heater for a series of tests was several hours).

15. The d-c supply voltage to the power amplifiers was reduced to the 5-kv level prior to extinguishing the plasma. This eliminated the possibility of induced thermal stress in the fused silica tubes due to a too-rapid high-power shut-down.

TABLE III

SUMMARY OF TEST CONDITIONS FOR DATA SHOWN IN FIGS. 11, 16, 19 AND 23

R-F Frequency mHz	Q_T (kw)	Plate Voltage (kv)	Total d-c Current (amps)	Resonator Voltage (Zero-to-Peak) (kv)	P_D (atm)	W_A (lb/sec)	d (in.)	A_s ($in.^2$)	V ($in.^3$)	$Q_{R,T}$ (kw)	Q_E (kw)	Q_L (kw)
5.5629	35.2	4.0	17.0	3.75	2.0	0.012	0.501	2.54	0.25	15.8	17.53	0.67
5.5659	38.3	5.0	12.75	3.84	2.0	0.010	0.560	2.85	0.32	16.1	20.24	0.66
5.5694	40.7	4.0	12.5	4.02	2.0	0.010	0.593	3.05	0.35	19.6	19.02	0.68
5.5902	43.2	4.0	12.5	4.43	2.0	0.010	0.719	3.64	0.53	21.6	19.23	0.81
5.5812	43.9	4.0	12.5	4.32	2.0	0.010	0.657	3.40	0.42	22.4	19.33	0.67
5.5991	44.9	4.0	12.5	4.32	2.0	0.010	0.750	3.89	0.58	24.2	18.52	0.68
5.5629	45.5	6.0	21.5	3.86	2.0	0.010	0.590	3.01	0.35	21.8	21.35	0.75
5.5761	49.4	5.0	16.0	4.32	2.0	0.012	0.610	3.14	0.38	24.2	22.66	0.84
5.5629	59.9	6.8	21.5	6.35	3.0	0.018	0.565	2.89	0.32	33.5	23.09	1.21
5.5629	65.2	9.0	30.5	8.26	4.0	0.023	0.595	3.05	0.36	40.7	20.96	1.34
5.5629	66.5	8.0	29.0	7.50	3.0	0.018	0.624	3.23	0.39	38.6	24.34	1.26
5.5629	73.5	9.0	30.5	8.65	5.0	0.023	0.562	2.85	0.32	47.1	22.35	1.55
5.5629	76.0	8.5	29.0	8.20	4.0	0.023	0.595	3.05	0.36	47.8	24.01	1.59
5.5629	78.6	9.0	29.0	9.40	4.0	0.026	0.547	2.77	0.30	45.6	38.63	1.67
5.5629	86.0	10.0	35.0	8.83	5.0	0.023	0.606	3.10	0.37	56.7	24.69	1.71
5.5629	91.0	10.0	35.0	9.12	6.0	0.023	0.596	3.05	0.36	65.2	21.50	1.90
5.5629	98.0	10.2	34.8	9.82	7.0	0.023	0.585	3.00	0.34	71.5	21.07	2.13
5.5629	103.5	10.5	34.5	10.80	8.0	0.023	0.572	2.92	0.33	78.1	19.69	2.21
5.5843	109.8	10.1	28.5	11.34	4.0	0.030	0.740	3.85	0.56	70.3	33.51	2.29
5.5773	116.7	11.0	27.5	12.48	7.0	0.033	0.640	3.30	0.42	87.5	22.85	2.35
5.5863	120.1	10.0	30.0	11.52	4.0	0.030	0.742	3.86	0.56	76.5	37.12	2.38
5.5629	134.7	10.8	34.4	11.52	9.0	0.023	0.545	2.76	0.30	103.7	24.07	2.43
5.5793	136.3	10.8	29.0	13.80	5.0	0.035	0.660	3.41	0.44	94.2	34.58	2.92
5.5629	139.8	11.0	34.4	12.10	11.0	0.023	0.516	2.60	0.27	112.5	20.09	2.51
5.5629	140.4	11.0	34.0	12.00	10.0	0.023	0.530	2.68	0.28	112.2	20.92	2.58
5.5629	141.3	11.0	34.0	12.30	12.0	0.025	0.501	2.52	0.25	115.0	18.87	2.63
5.5728	144.5	11.6	27.0	15.70	17.5	0.027	0.520	2.62	0.27	121.5	15.12	2.98
5.5700	159.8	12.8	27.5	17.10	19.2	0.027	0.530	2.68	0.28	131.1	20.11	3.29
5.5873	223.4	14.5	39.1	16.32	7.0	0.033	0.750	3.89	0.58	162.0	49.60	4.30

TABLE IV

COMPARISON OF OPERATING CONDITIONS IN FULL-SCALE ENGINE AND EARLY IN-REACTOR TEST CONFIGURATION WITH THOSE IN 1.2-MEGW R-F INDUCTION HEATER RADIANT ENERGY SOURCE

Full-Scale Engine Data Obtained from Ref. 1

In-Reactor Test Configuration Data Obtained from Ref. 11

	Unit Cavity of Full-Scale Engine		Early In-Reactor Test Configuration	R-F Plasma Radiant Energy Source
	Reference Engine	Derated Engine		
Transparent-wall configuration	Circumferential Tubes	Circumferential Tubes	Circumferential Tubes	Concentric Tubes
Inside diameter, ft	1.604	1.604	0.262	0.187
Length between containing end walls, ft	6.0	6.0	0.70	0.167
Length/Diameter ratio	3.75	3.75	2.68	0.893
Cylindrical surface area, sq ft	30.2	30.2	0.576	0.147*
Coolant fluid	Hydrogen	Hydrogen	Hydrogen-Argon	Water
Buffer fluid	Neon	Neon	Argon	Argon
Buffer injection velocity, ft/sec	25**	25**	9.6	10-50
Buffer weight flow, lb/sec	2.96	2.96	0.064	0.01-0.04
Chamber pressure, atm	500	500	500	1-20
Equivalent black-body radiating temperature, R	15,000	8000	7040	10,860
Radiant heat flux per unit area, Btu/sec-sq ft	24,300	1944	1130	6660
kw/sq in.	178	14.4	8.36	49.0
Total heat flux deposited in wall, Btu/sec-sq ft	490	39.2	580	110

*Based on 3-in. length.

**Assumed value of $v_l/v_j = 0.4$.

NUCLEAR LIGHT BULB ENGINE CONCEPT AND R-F PLASMA RADIANT ENERGY SOURCE

(a) SCHEMATIC OF UNIT CAVITY OF NUCLEAR LIGHT BULB ENGINE

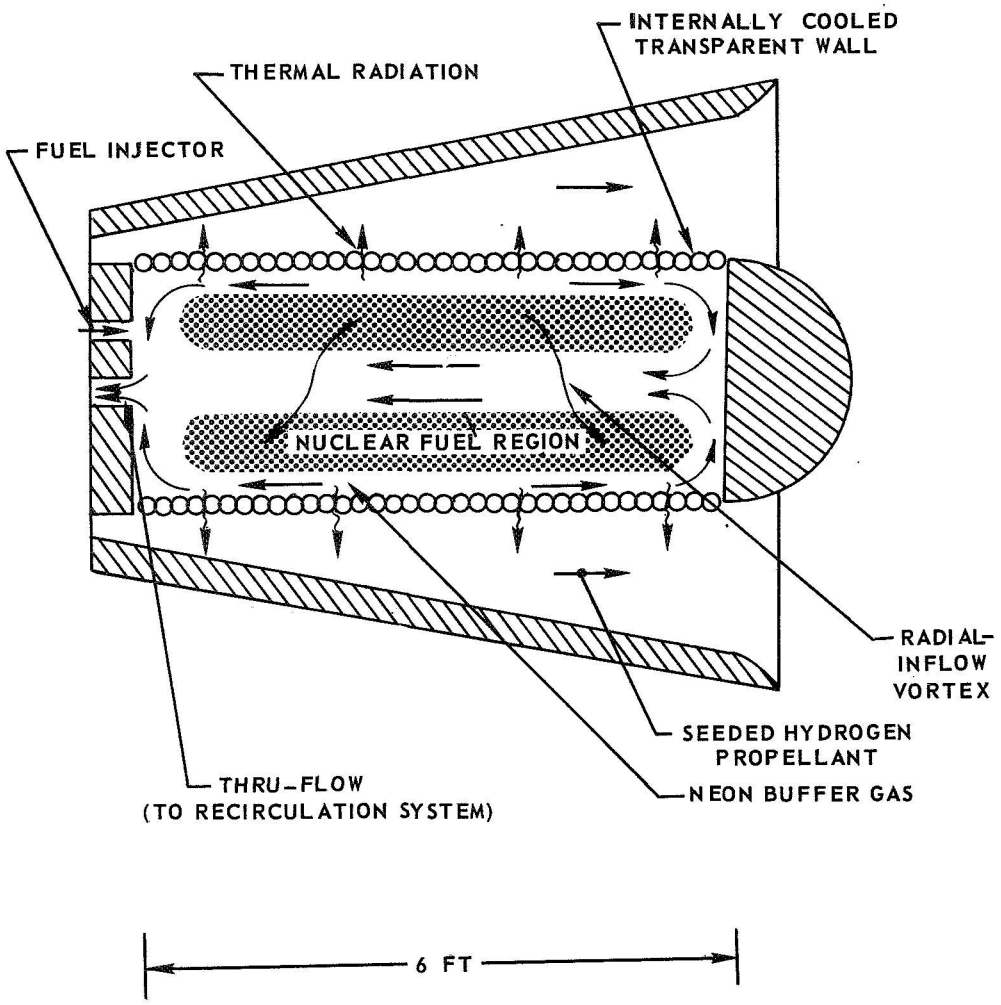

(b) SCHEMATIC OF R-F PLASMA RADIANT ENERGY SOURCE

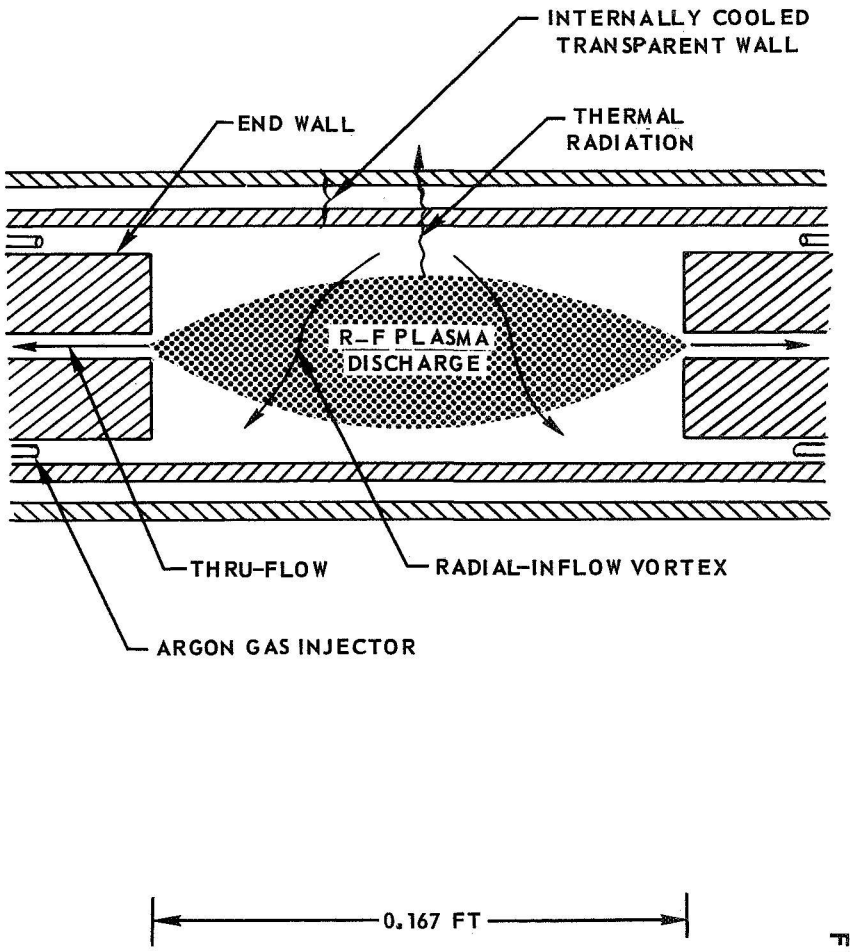

FIG. 1

BLOCK DIAGRAM OF UARL 1.2 – MEGW R-F INDUCTION HEATER

POWER LEVELS SHOWN ARE MAXIMUM DESIGN VALUES

MAXIMUM TOTAL D-C INPUT POWER DURING THIS PROGRAM FOR POWER AMPLIFIERS 1 AND 2 WAS APPROXIMATELY 650 KW

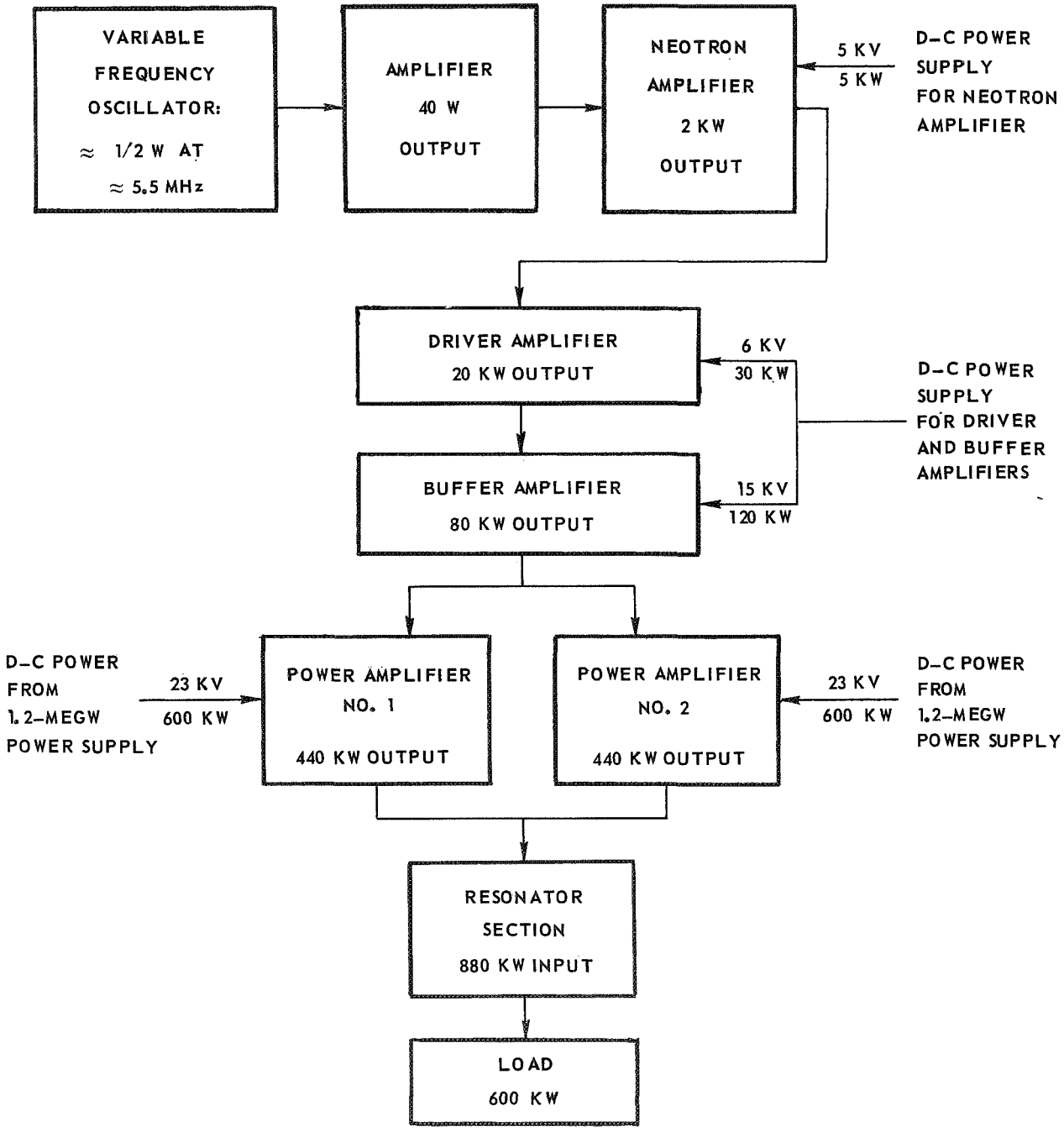

PHOTOGRAPH OF 1.2-MEGW R-F INDUCTION HEATER RESONATOR SECTION AND TEST CHAMBER

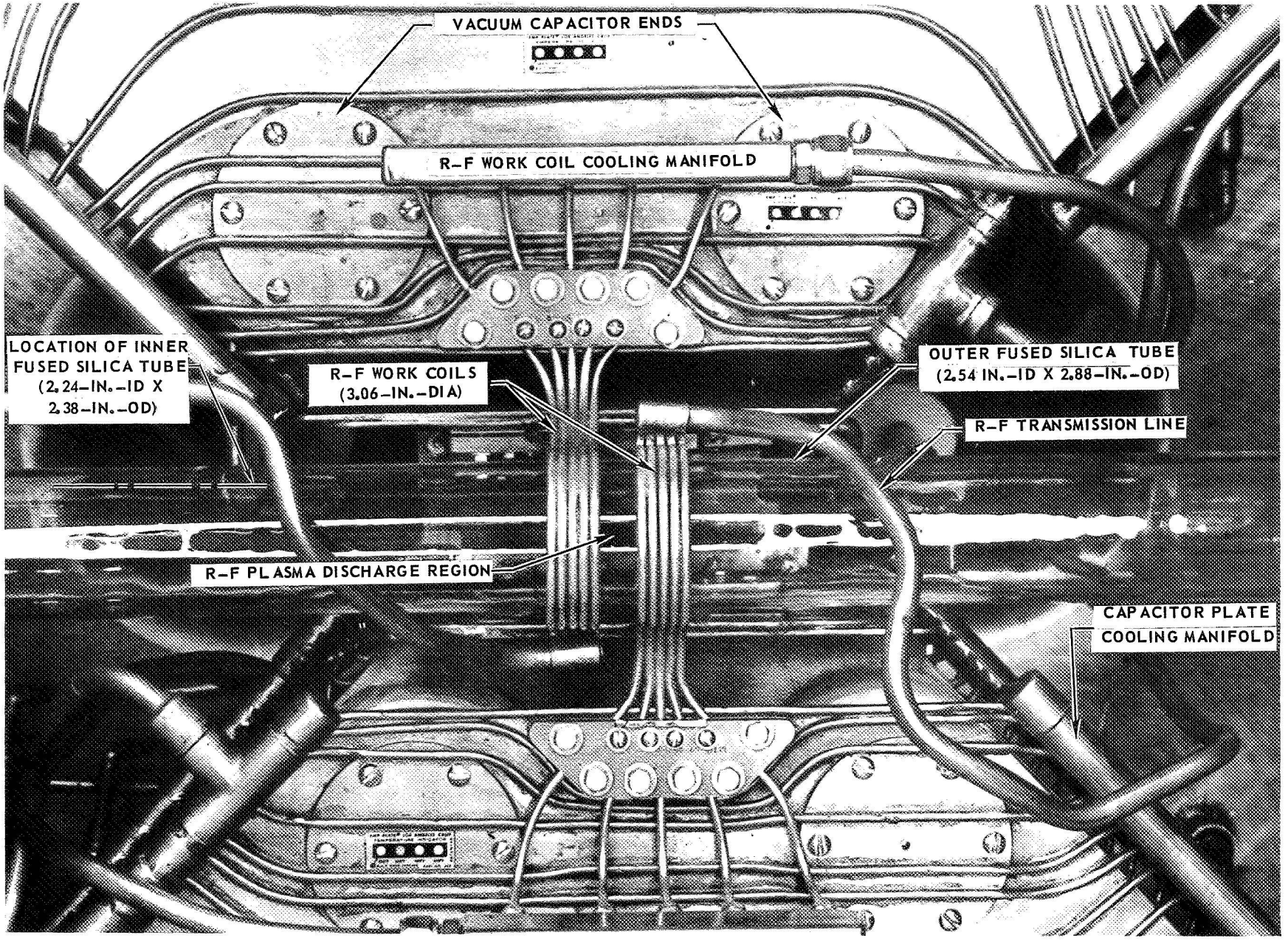

J-910900-4

FIG. 3

PHOTOGRAPH OF CONTROL CONSOLES USED IN RADIANT ENERGY SOURCE TESTS
1.2-MEGW R-F INDUCTION HEATER

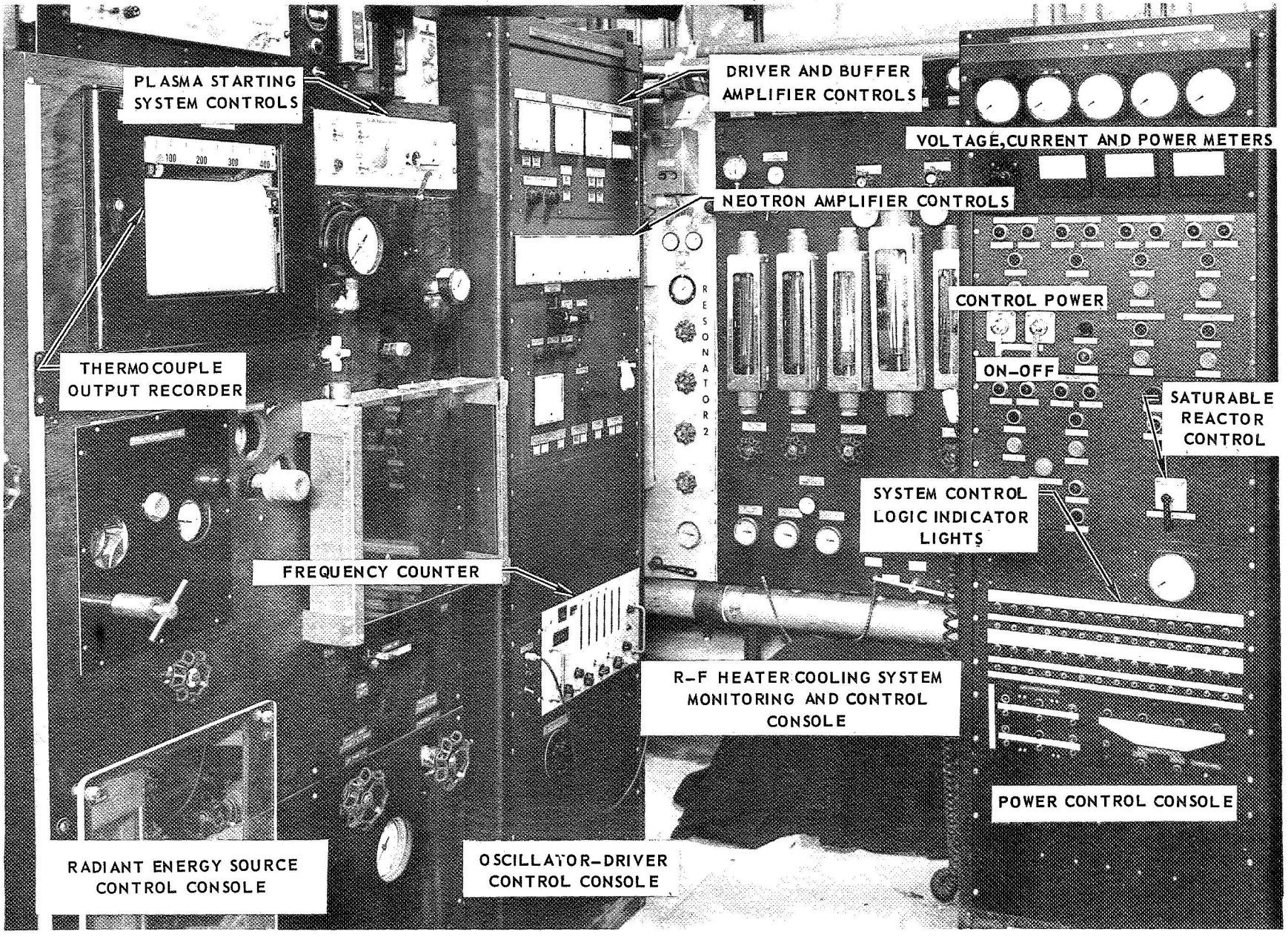

BLOCK DIAGRAM OF ARGON GAS INJECTION AND EXHAUST SYSTEM

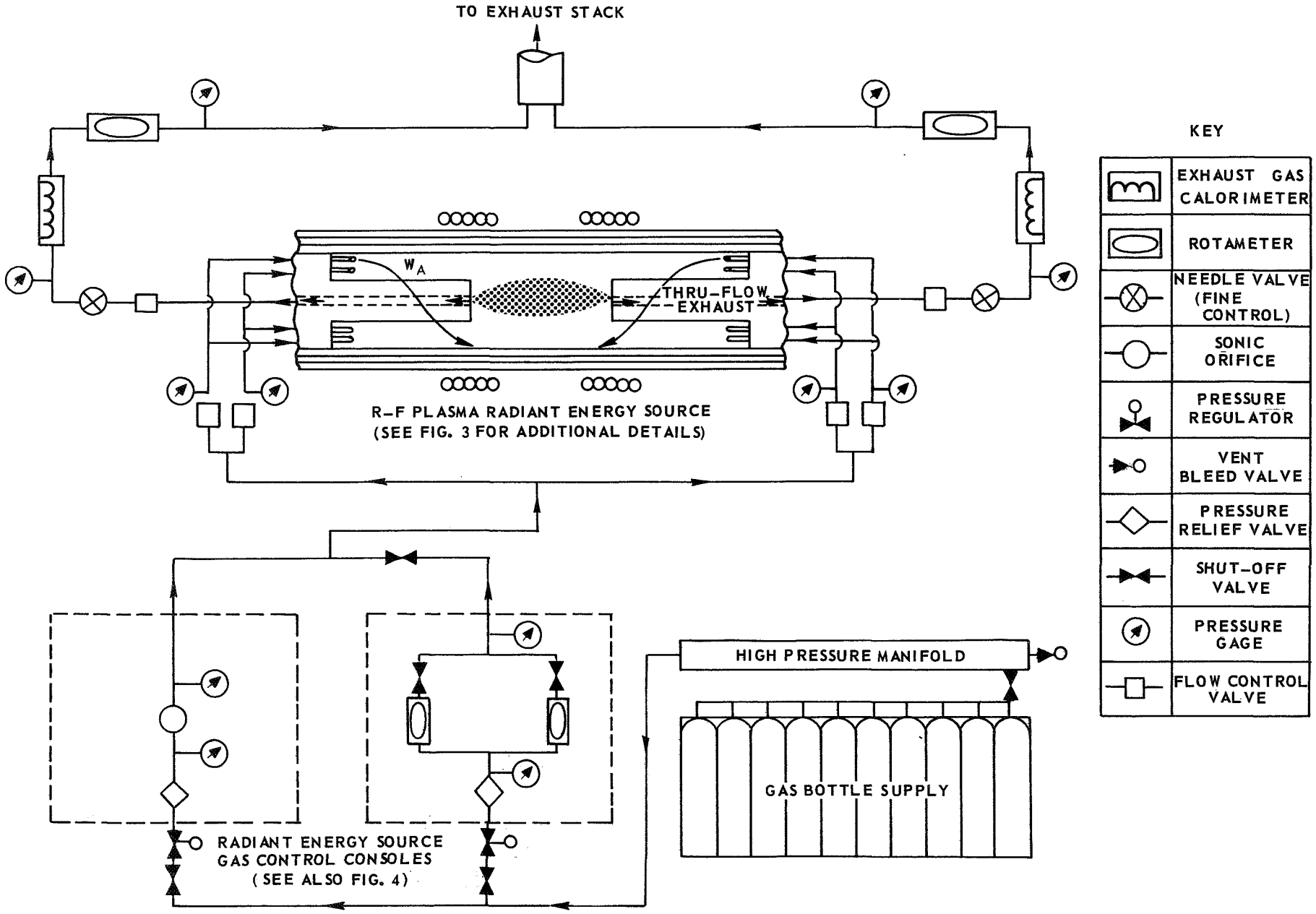

J-910900-4

FIG. 5

TRANSMISSION CHARACTERISTICS OF RADIOMETER OPTICAL SYSTEM AND TYPICAL OSCILLOSCOPE OUTPUT TRACE

SEE REF. 15 FOR OPTICAL SYSTEM DETAILS

(a) TRANSMISSION CHARACTERISTICS OF RADIOMETER OPTICAL SYSTEM

NOTE: ALL CUT-OFFS SHOWN AT 50 PERCENT TRANSMISSION LEVEL

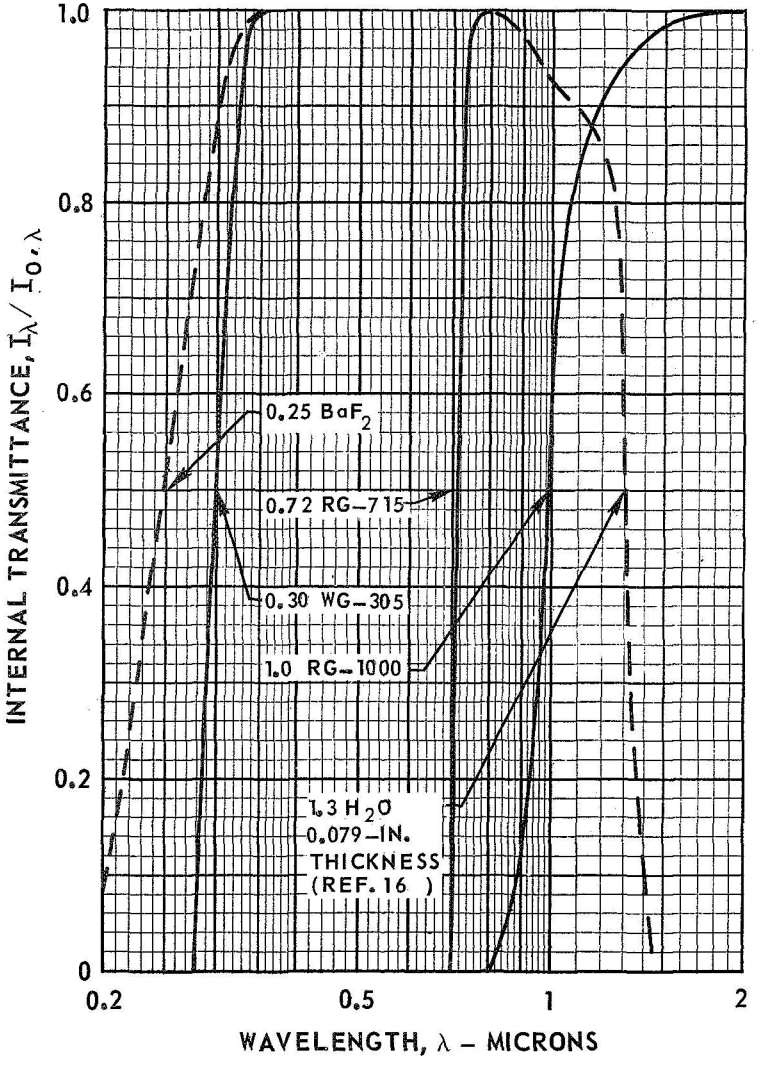

(b) TYPICAL OSCILLOSCOPE TRACE OF RADIOMETER OUTPUT IN VARIOUS WAVELENGTH BANDS

SOURCE – TUNGSTEN FILAMENT STANDARD LAMP (DXW)

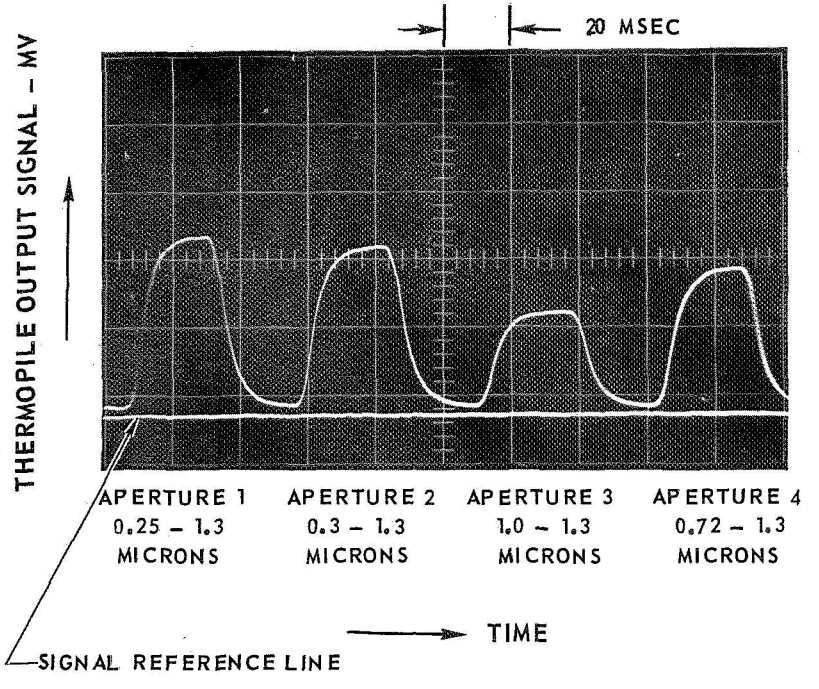

FIG. 7

EFFECT OF DYE CONCENTRATION ON RADIATION ATTENUATION IN PERIPHERAL-WALL COOLANT

DATA FOR NIGROSINE DYE IN WATER FLOWING THROUGH COOLANT ANNULUS

SEE FIG. 3 FOR DETAILS OF TEST CONFIGURATION

SEE FIG. 6 FOR TRANSMISSION CHARACTERISTICS OF RADIOMETER SYSTEM

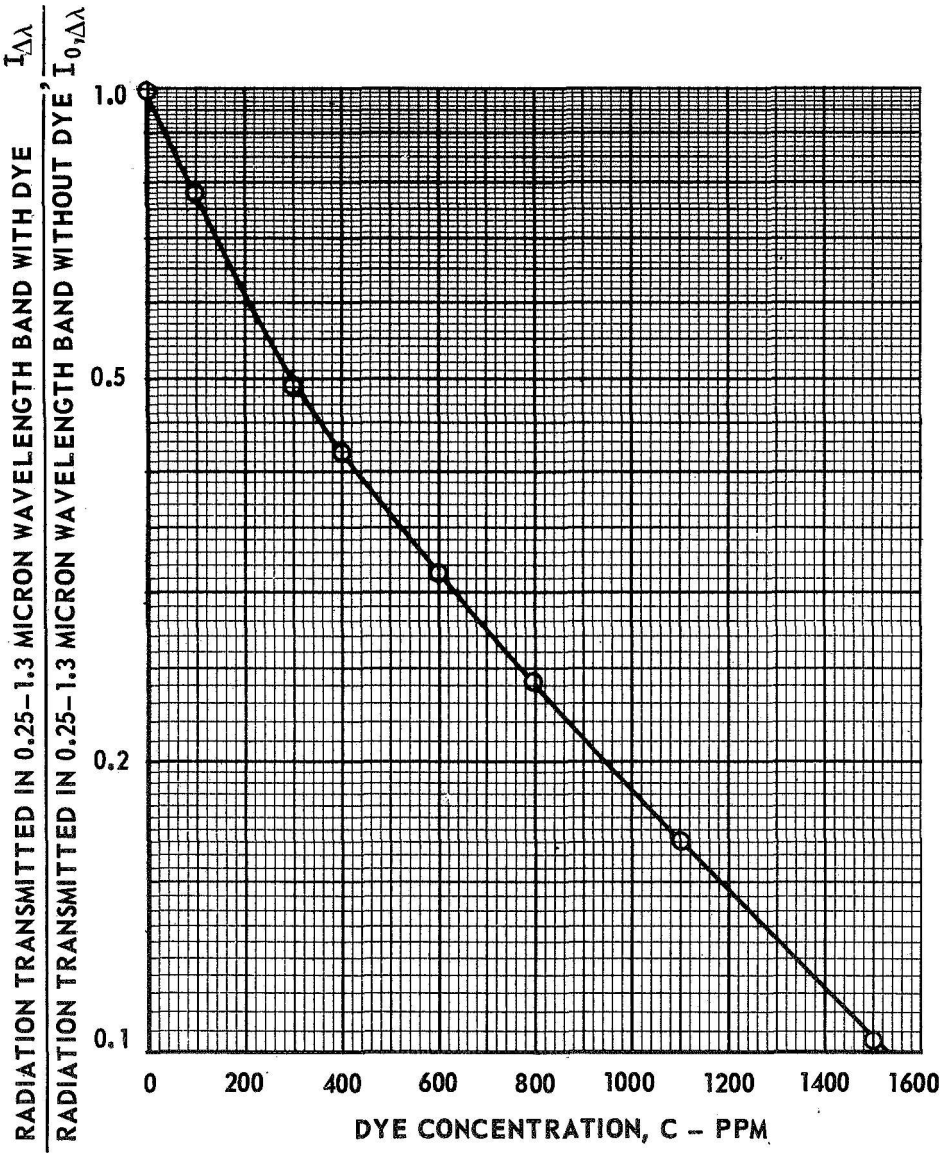

FIG. 8

SKETCHES OF RADIANT ENERGY SOURCE CONFIGURATIONS USED IN 1.2-MEGW R-F INDUCTION HEATER

CONFIGURATIONS SHOWN APPROXIMATELY FULL SIZE

(a) CONFIGURATION HAVING 16 VORTEX INJECTORS AT TWO RADIAL LOCATIONS

SEE FIG. 9 FOR FURTHER DETAILS OF VORTEX INJECTOR MANIFOLD

SEE FIG. 5 FOR FURTHER DETAILS OF ARGON INLET AND EXHAUST SYSTEM

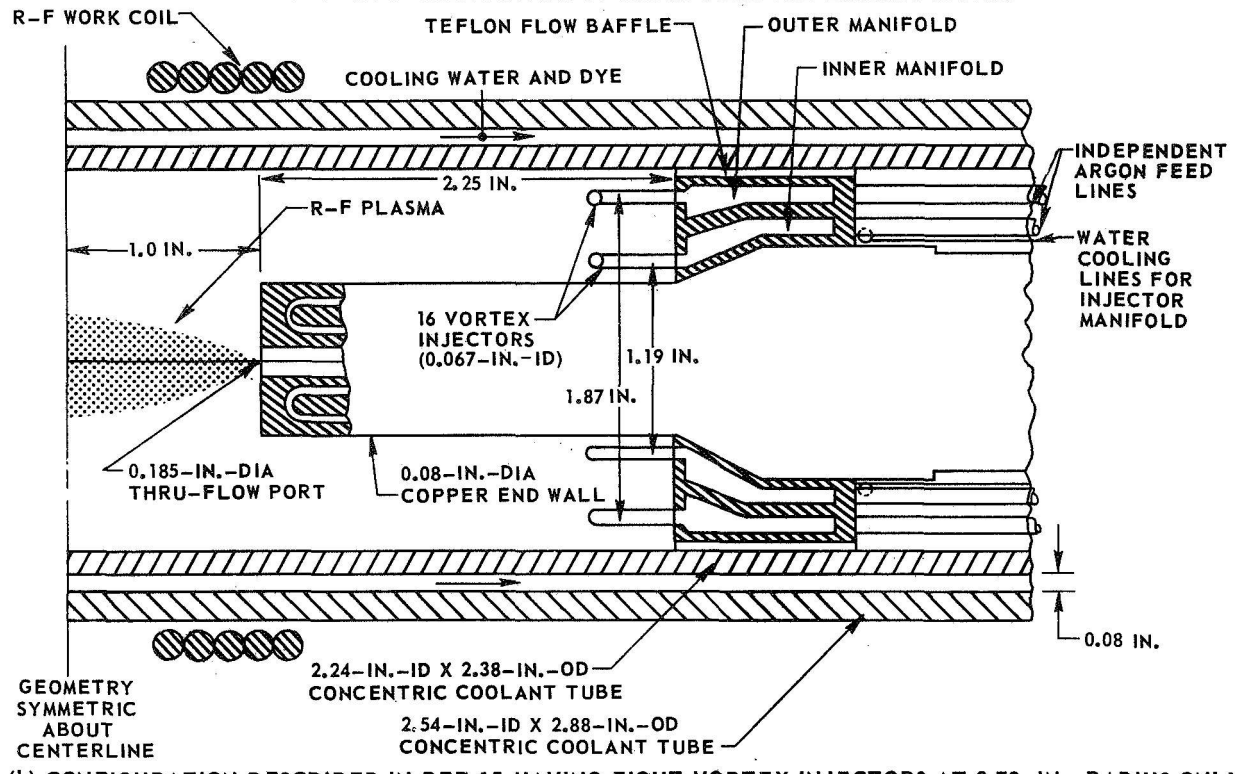

(b) CONFIGURATION DESCRIBED IN REF.15 HAVING EIGHT VORTEX INJECTORS AT 0.72-IN.-RADIUS ONLY

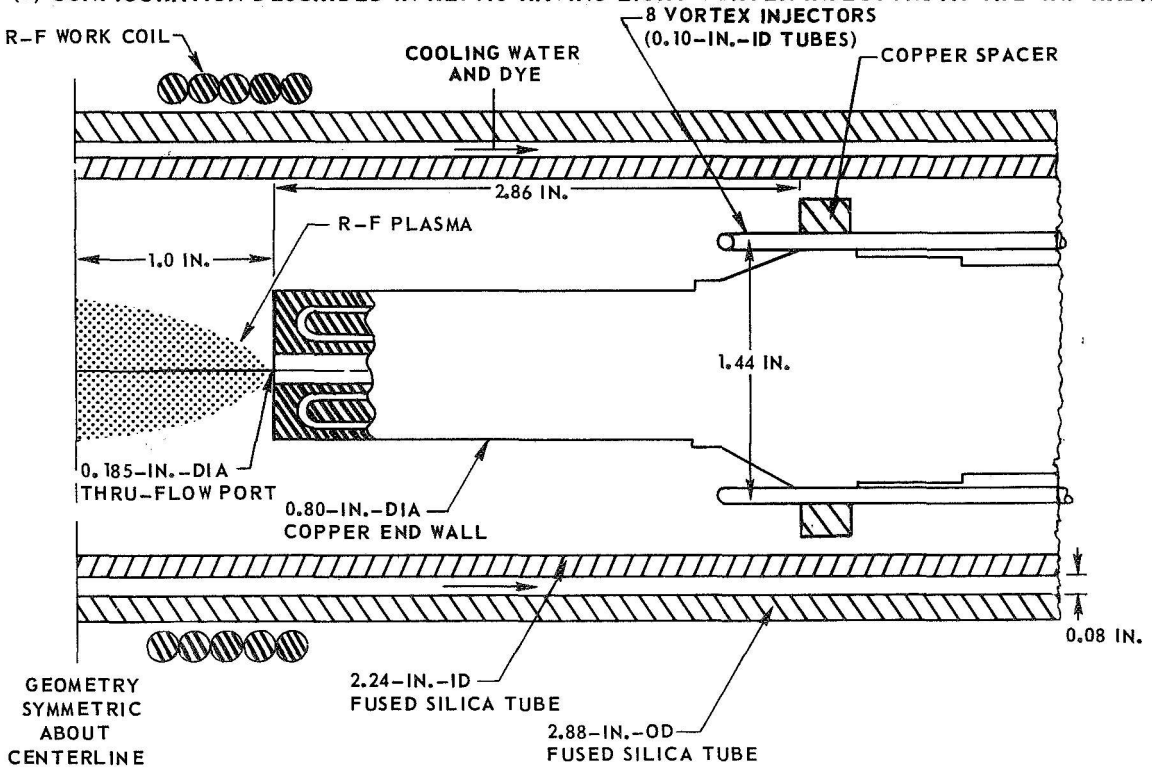

DETAILS OF VORTEX MULTIPLE – INJECTOR MANIFOLD HAVING 16 VORTEX INJECTORS AT TWO RADIAL LOCATIONS

☆ STAR SYMBOLS INDICATE APPROXIMATE LOCATIONS OF "TEMPILAC" TEMPERATURE SENSITIVE PAINTS OF VARIOUS RANGES (FROM 200 TO 500F USED IN SOME TESTS)

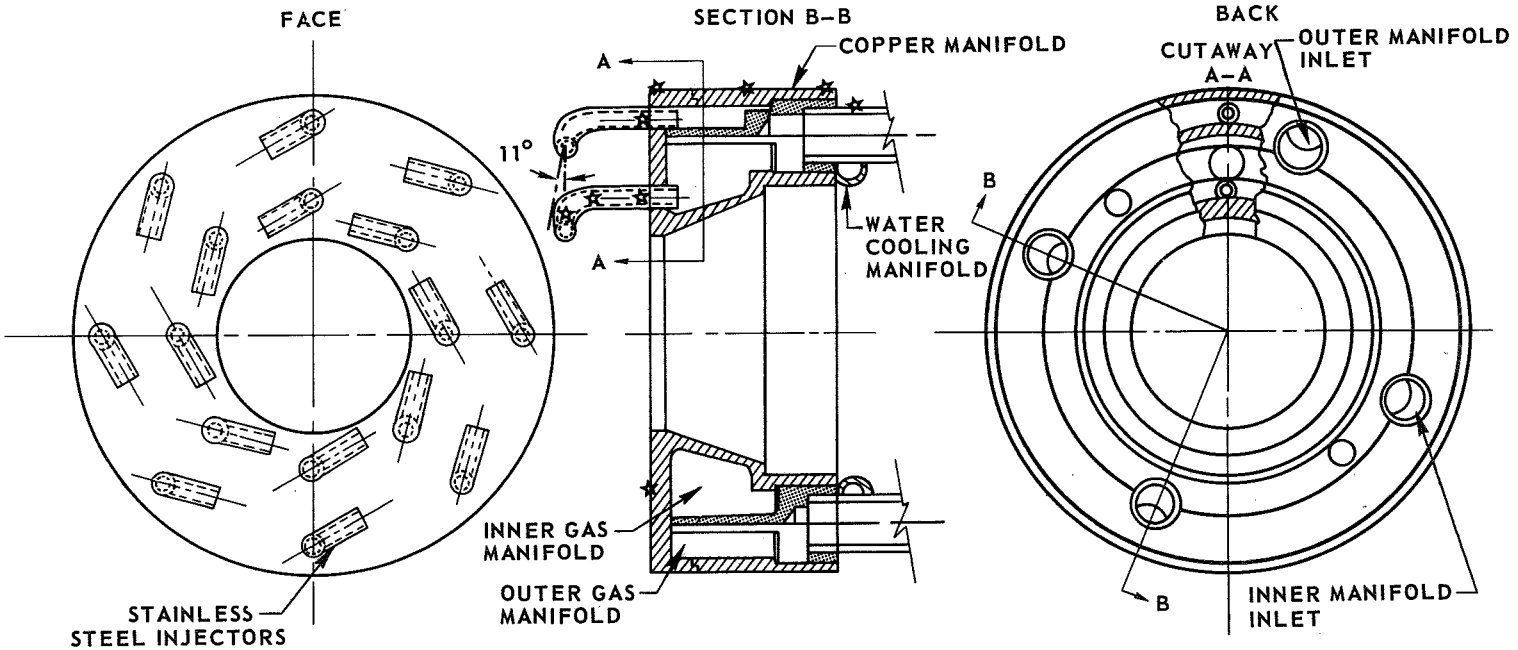

SKETCH OF RADIANT ENERGY SOURCE SHOWING POWER BREAKDOWN

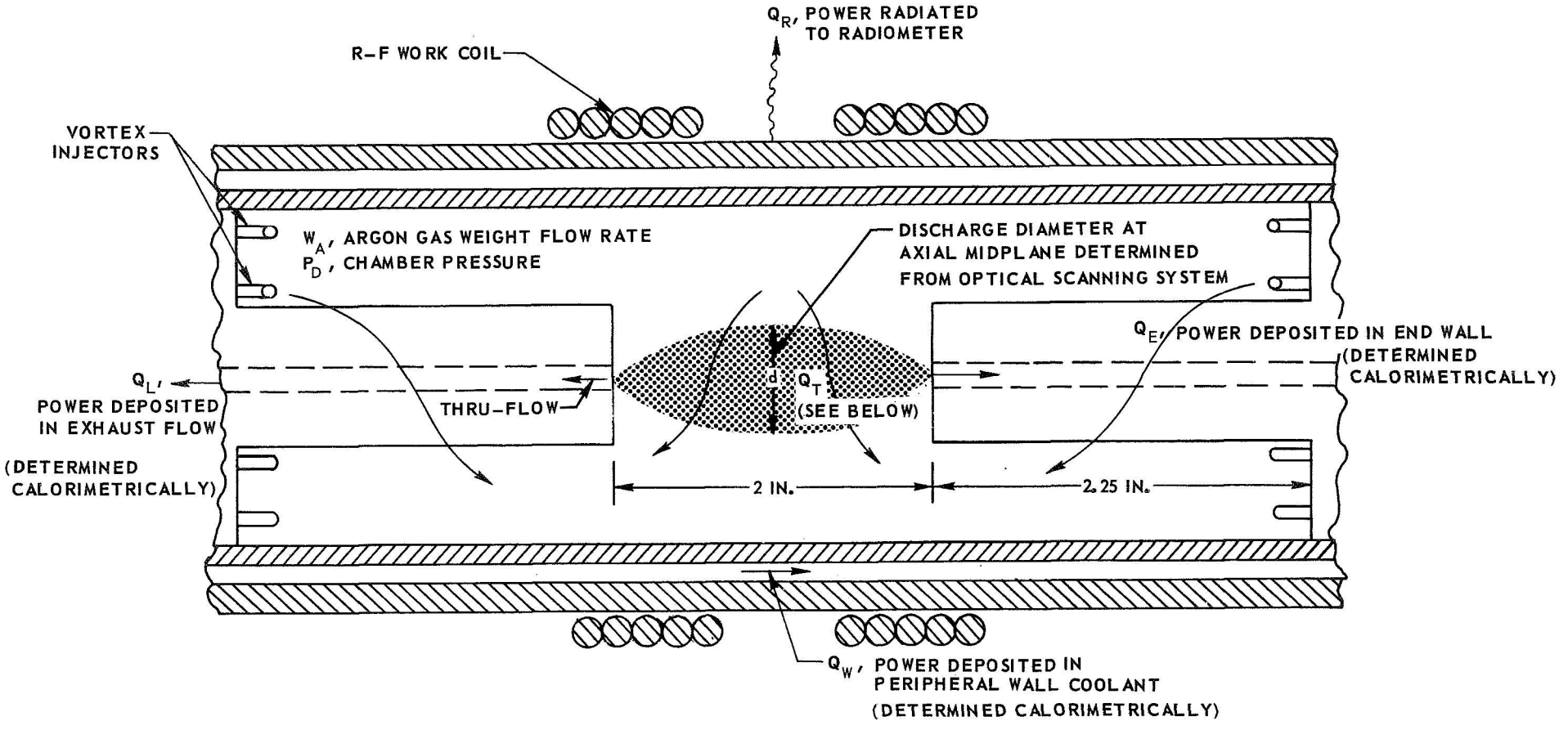

TOTAL POWER DEPOSITED IN R-F PLASMA DISCHARGE, $Q_T = Q_R + Q_W + Q_E + Q_L$

FIG. 10

FIG. 11

VARIATION OF GEOMETRIC CHARACTERISTICS OF ARGON R-F PLASMA DISCHARGE WITH TOTAL DISCHARGE POWER

▲ CONFIGURATION HAVING 16 VORTEX INJECTORS AT TWO RADIAL LOCATIONS
SEE FIG. 8 (a) FOR DETAILS OF TEST CONFIGURATION
RANGE OF CHAMBER PRESSURE, P_D = 2 TO 19.2 ATM
RANGE OF ARGON WEIGHT FLOW, W_A = 0.010 TO 0.035 LB/SEC
RANGE OF R-F FREQUENCY, f = 5.5629 TO 5.5991 MHz

○ CONFIGURATION HAVING 8 VORTEX INJECTORS AT 0.72-IN. RADIUS
SEE FIG. 8 (b) AND REF. 15 FOR DETAILS OF TEST CONFIGURATION AND DATA

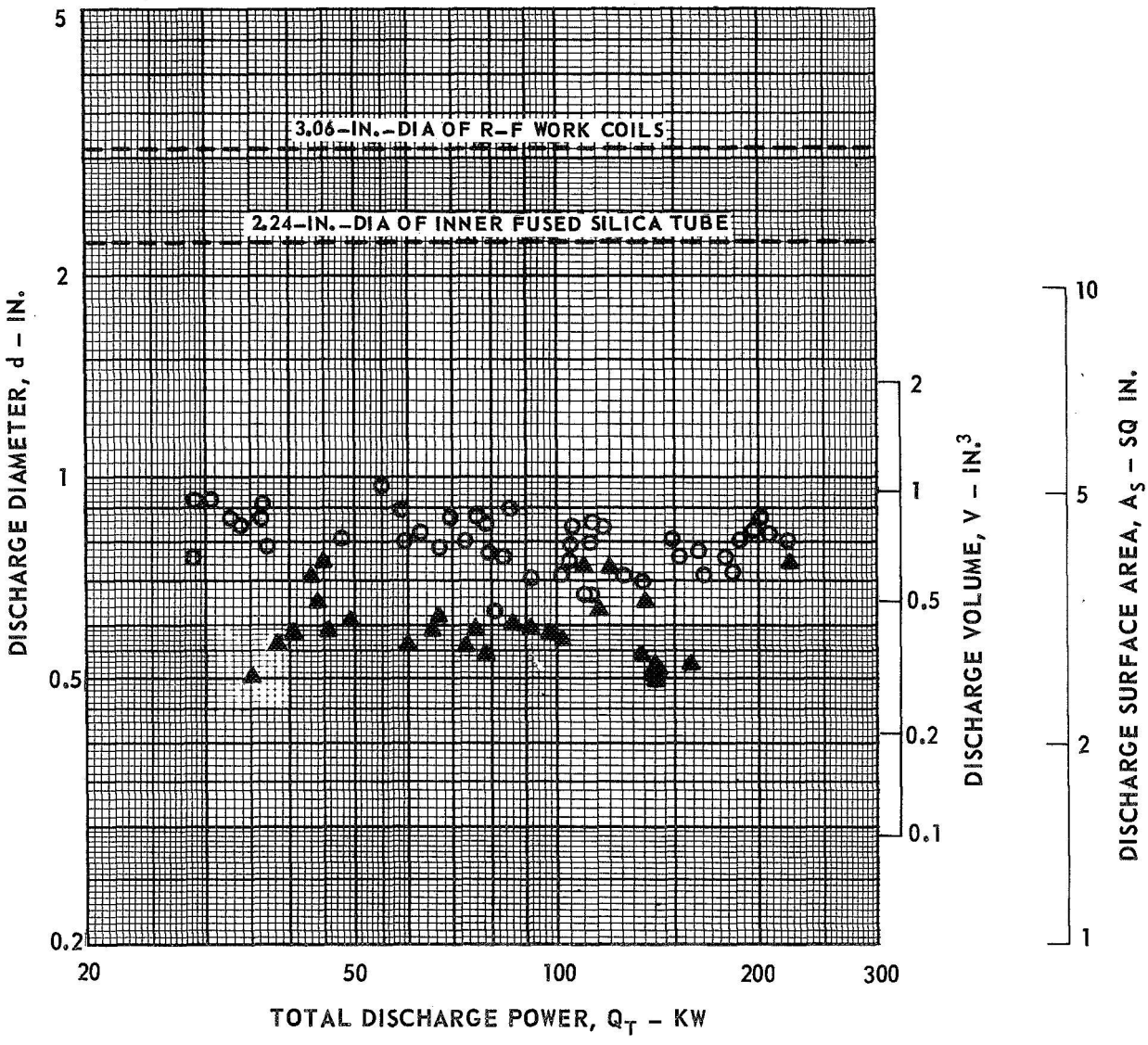

EFFECT OF R-F OPERATING FREQUENCY ON DISCHARGE GEOMETRIC CHARACTERISTICS AND POWER DEPOSITION

SEE FIG. 8 (a) FOR DETAILS OF TEST CONFIGURATION

ARGON WEIGHT FLOW, $W_A = 0.008$ LB/SEC

CHAMBER PRESSURE, $P_D = 4$ ATM

TOTAL DISCHARGE POWER, $Q_T \approx 15$ KW

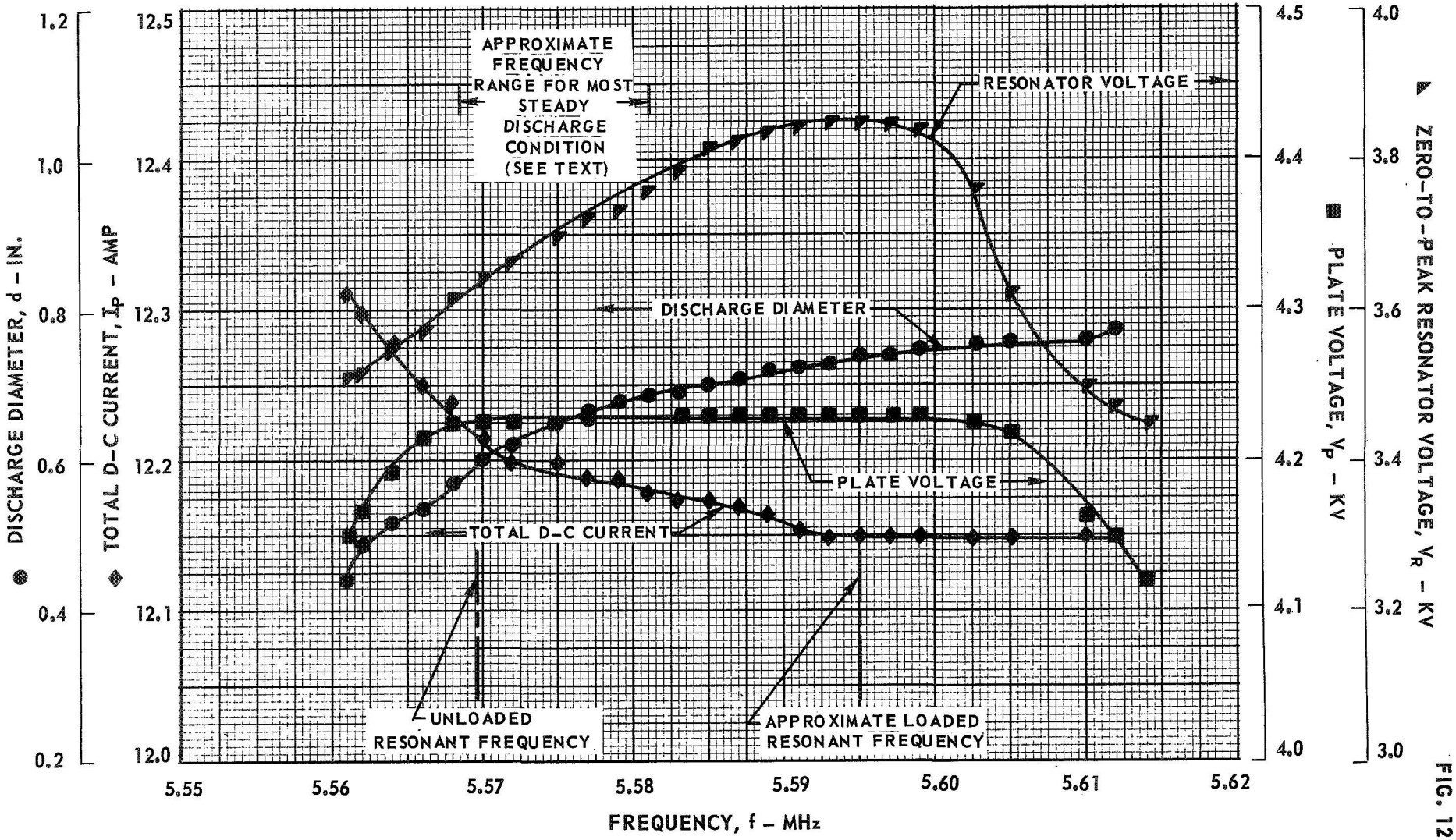

FIG. 12

J-910900-4

SKETCH OF RADIANT ENERGY SOURCE CONFIGURATION SHOWING POWER LOSSES FOR HIGHEST POWER OPERATING POINT

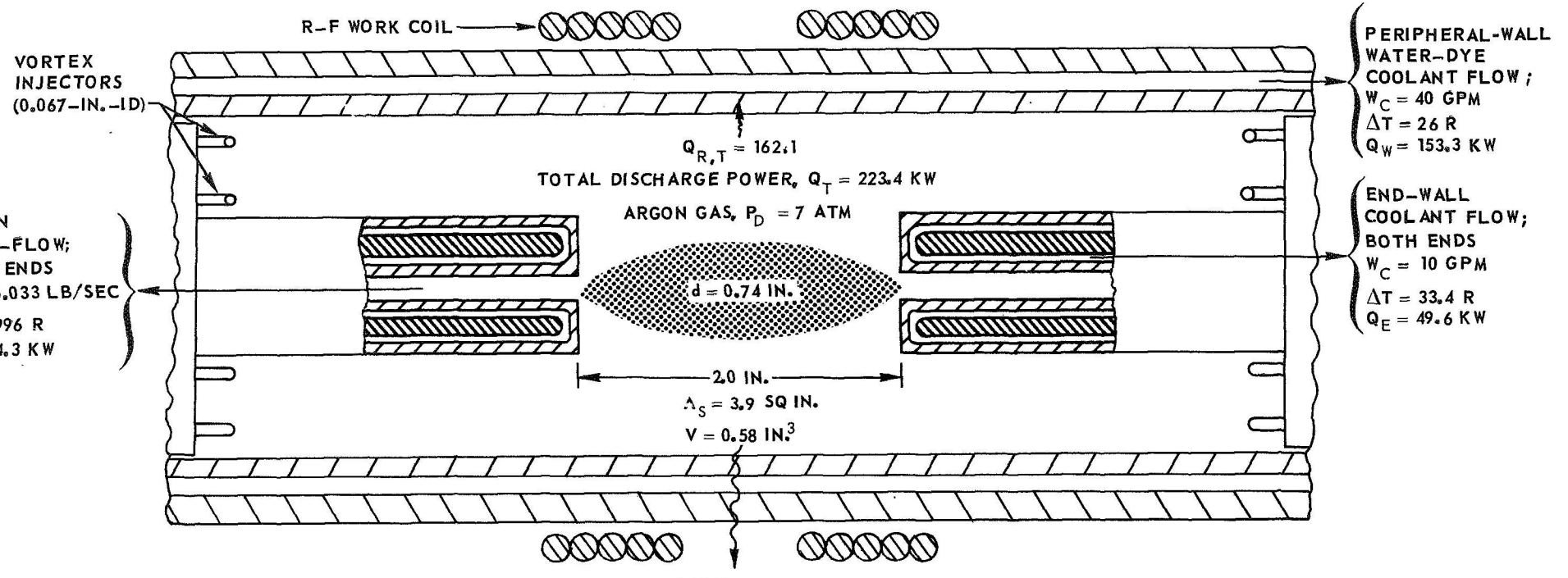

READING = 1884 MV

$Q_R = (8.6 \times 10^{-3}\ KW/MV)\ (1884\ MV) = 16.2\ KW$

TOTAL D-C INPUT POWER, Q_I = 640 KW AT 5.5873 MHz

TOTAL DISCHARGE POWER, $Q_T = 16.2 + 153.4 + 49.6 + 4.3 = 223.4$ KW

R-F SYSTEM COUPLING EFFICENCY, $\eta = 223.4/640 = 34.9$ PERCENT

PROBABLE MAXIMUM POWER CONDUCTED THROUGH PERIPHERAL WALL, Q_C = 7.5 KW

TOTAL POWER RADIATED THROUGH INNER PERIPHERAL WALL, $Q_{R,T} = 153.4 - 7.5 + 16.2 = 162.1$

$\phi_R = Q_{R,T}/A_S = 162.1/3.9 = 41.5$ KW/SQ IN. ($T^* = 10,420$ R)

FRACTION OF DISCHARGE POWER RADIATED THROUGH INNER PERIPHERAL WALL, $Q_{R,T}/Q_T = 162.1/223.4 = 0.72$

FIG. 13

SKETCH OF SEPARATELY COOLED END-WALL FACE CAP EMPLOYED IN 1.2 – MEGW R-F RADIANT ENERGY SOURCE TESTS

☆ STAR SYMBOLS INDICATE APPROXIMATE LOCATIONS OF "TEMPILAC" TEMPERATURE SENSITIVE PAINTS OF VARIOUS RANGES (FROM 200 TO 500F USED IN SOME TESTS)

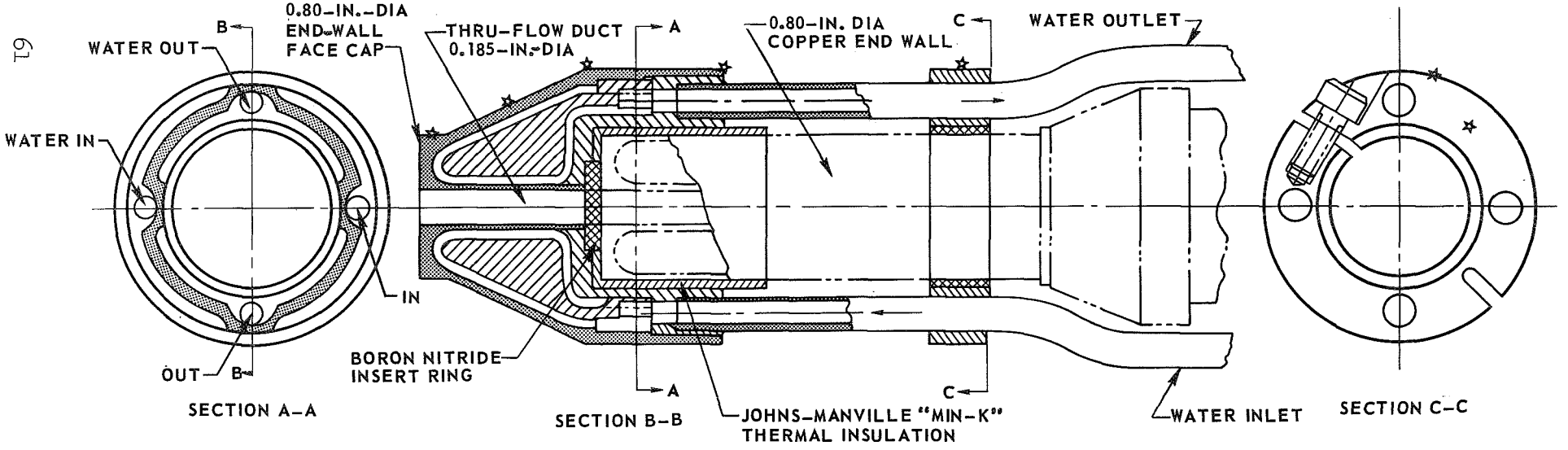

FIG. 14

CONFIGURATION AND RESULTS OF TEST EMPLOYING SEPARATELY COOLED END-WALL FACE CAP

SEE FIG. 14 FOR DETAILS OF END-WALL FACE CAP

(a) PHOTOGRAPH OF END-WALL FACE CAP AND VORTEX INJECTOR MANIFOLD MOUNTED ON 0.80-IN.-DIA END WALLS

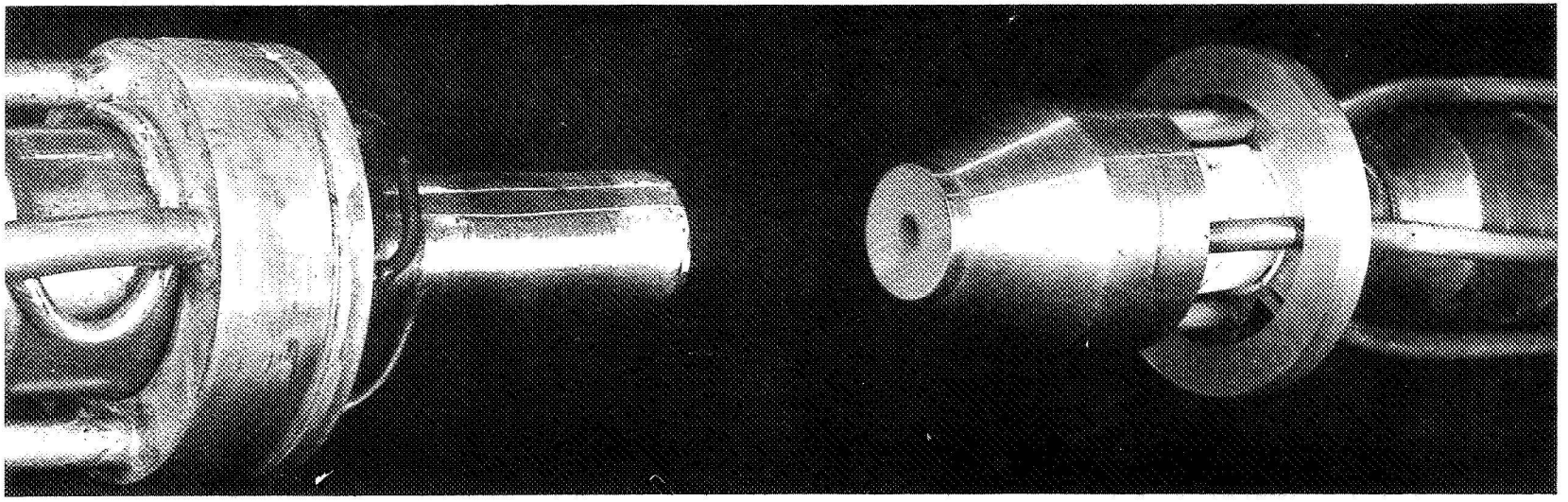

(b) POWER LOSS BREAKDOWN

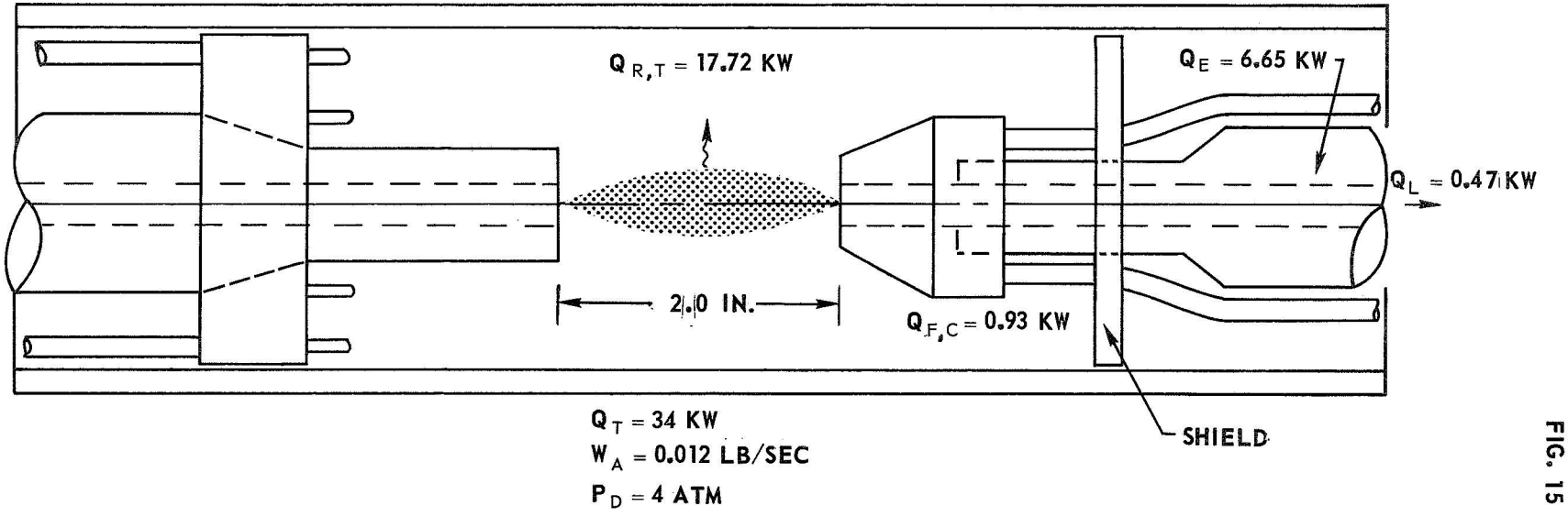

Q_T = 34 KW
W_A = 0.012 LB/SEC
P_D = 4 ATM

FIG. 15

FIG. 16

VARIATION OF DISCHARGE POWER PER UNIT VOLUME WITH TOTAL DISCHARGE POWER

▲ CONFIGURATION HAVING 16 VORTEX INJECTORS AT TWO RADIAL LOCATIONS

SEE FIG. 8 (a) FOR DETAILS OF TEST CONFIGURATION

RANGE OF CHAMBER PRESSURE, P_D = 2 TO 19.2 ATM

RANGE OF ARGON WEIGHT FLOW, W_A = 0.010 TO 0.035 LB/SEC

RANGE OF R-F OPERATING FREQUENCY, f = 5.5629 TO 5.5991 MHz

○ CONFIGURATION HAVING 8 VORTEX INJECTORS AT 0.72-IN.-RADIUS

SEE FIG. 8 (b) AND REF. 15 FOR DETAILS OF TEST CONFIGURATION AND DATA

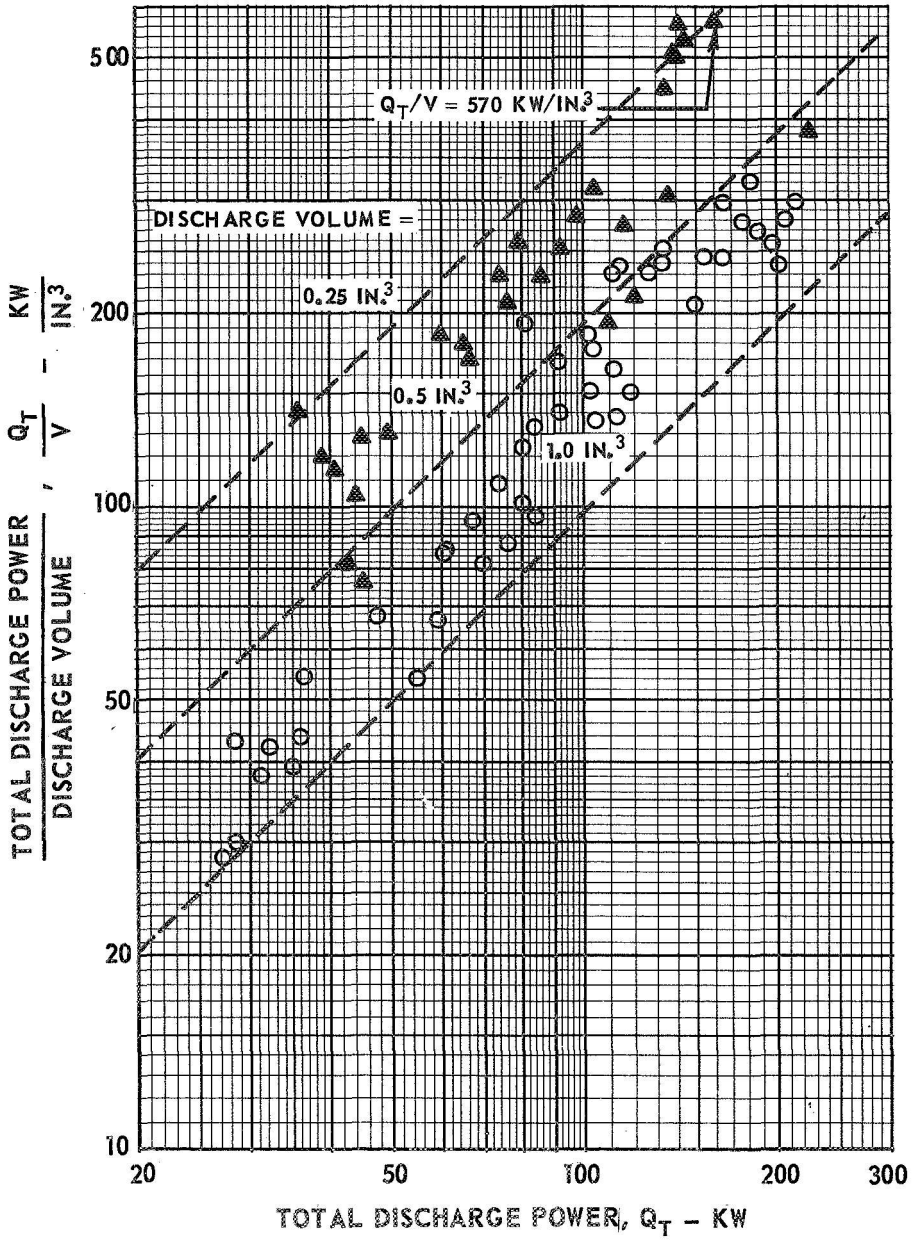

VARIATION OF RADIANT ENERGY FLUX WITH TOTAL DISCHARGE POWER

▲ CONFIGURATION HAVING 16 VORTEX INJECTORS AT TWO RADIAL LOCATIONS
SEE FIG. 8 (a) FOR DETAILS OF TEST CONFIGURATION
RANGE OF CHAMBER PRESSURE, P_D = 2 TO 19.2 ATM
RANGE OF ARGON WEIGHT FLOW, W_A = 0.010 TO 0.035 LB/SEC
RANGE OF R-F OPERATING FREQUENCY, f = 5.5629 TO 5.5991 MHz

○ CONFIGURATION HAVING 8 VORTEX INJECTORS AT 0.72-IN. RADIUS
SEE FIG. 8 (b) AND REF. 15 FOR DETAILS OF TEST CONFIGURATION AND DATA

$$\phi_R = Q_{R,T} / A_S$$

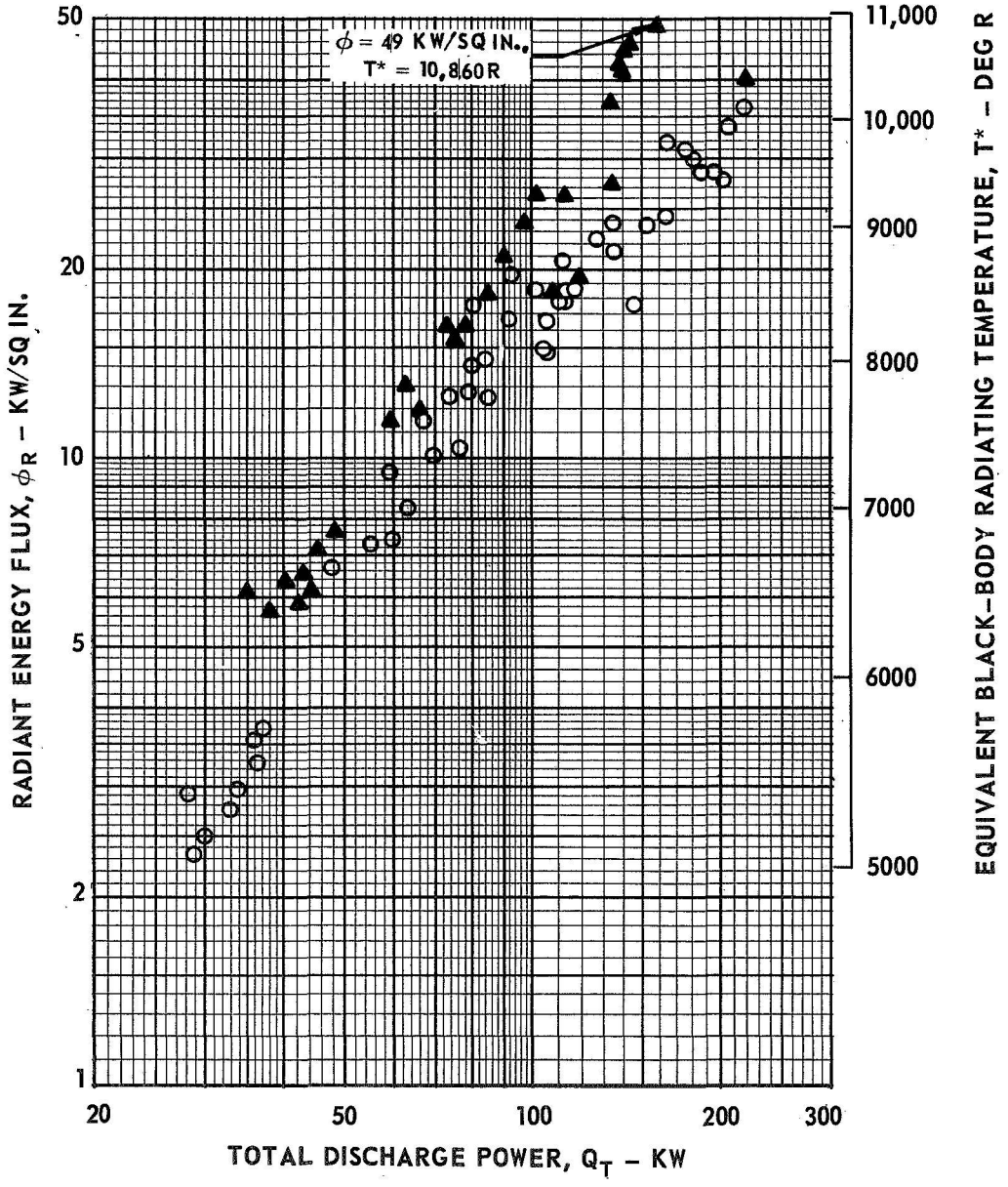

EFFECT OF R-F OPERATING FREQUENCY ON DISCHARGE POWER AND RADIATION CHARACTERISTICS

SEE FIG. 8 (a) FOR DETAILS OF TEST CONFIGURATION

ARGON WEIGHT FLOW, $W_A = 0.008$ LB/SEC

CHAMBER PRESSURE, $P_D = 4$ ATM

TOTAL DISCHARGE POWER, $Q_T \approx 15$ KW

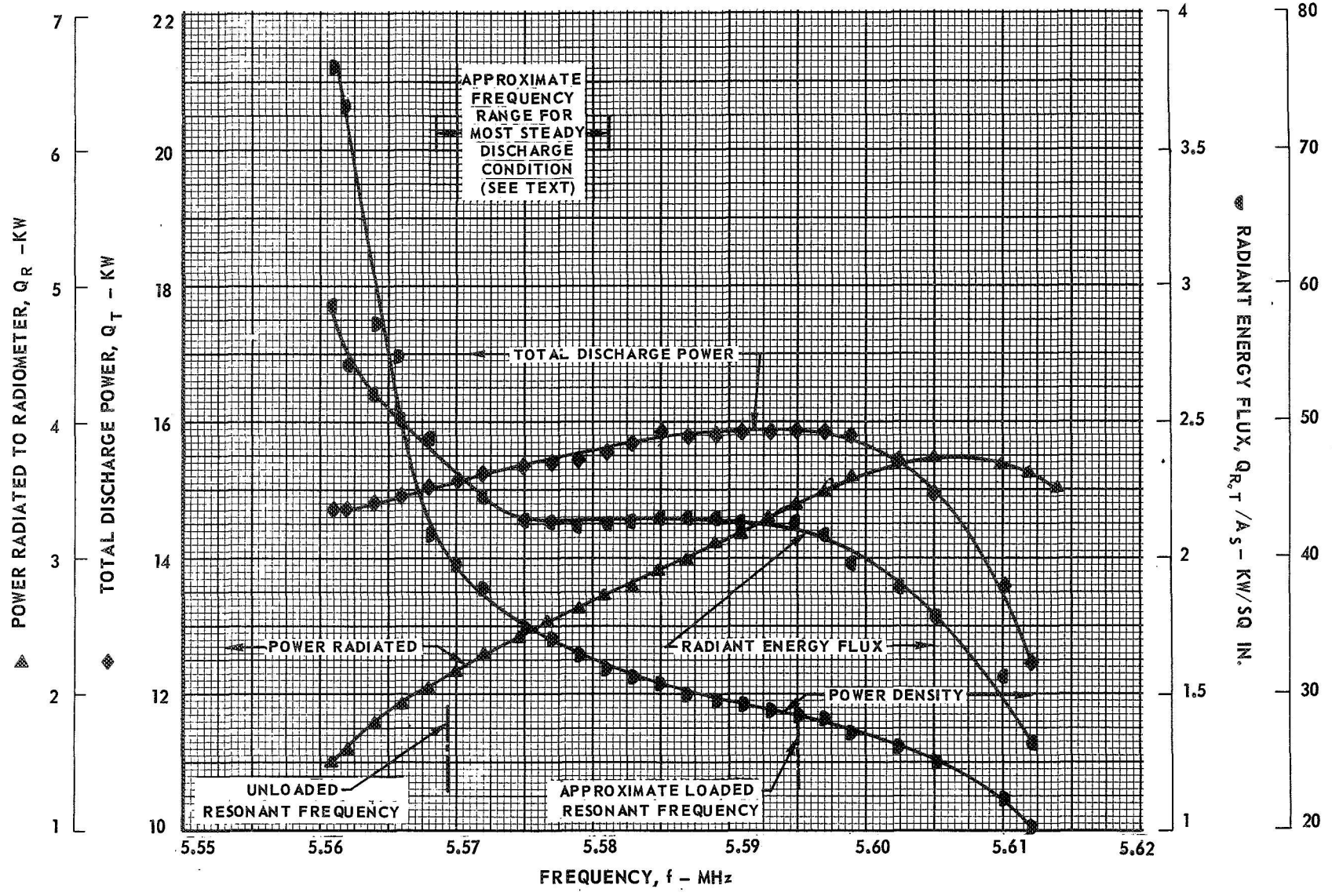

FIG. 18

EFFECT OF CHAMBER PRESSURE ON RADIATED POWER EFFICIENCY

SEE FIG. 8 (a) FOR DETAILS OF TEST CONFIGURATION

RANGE OF TOTAL DISCHARGE POWER, Q_T = 60 TO 160 KW

RANGE OF ARGON WEIGHT FLOW, W_A = 0.018 TO 0.035 LB/SEC

RANGE OF R-F OPERATING FREQUENCY, f = 5.5629 TO 5.5793 MHz

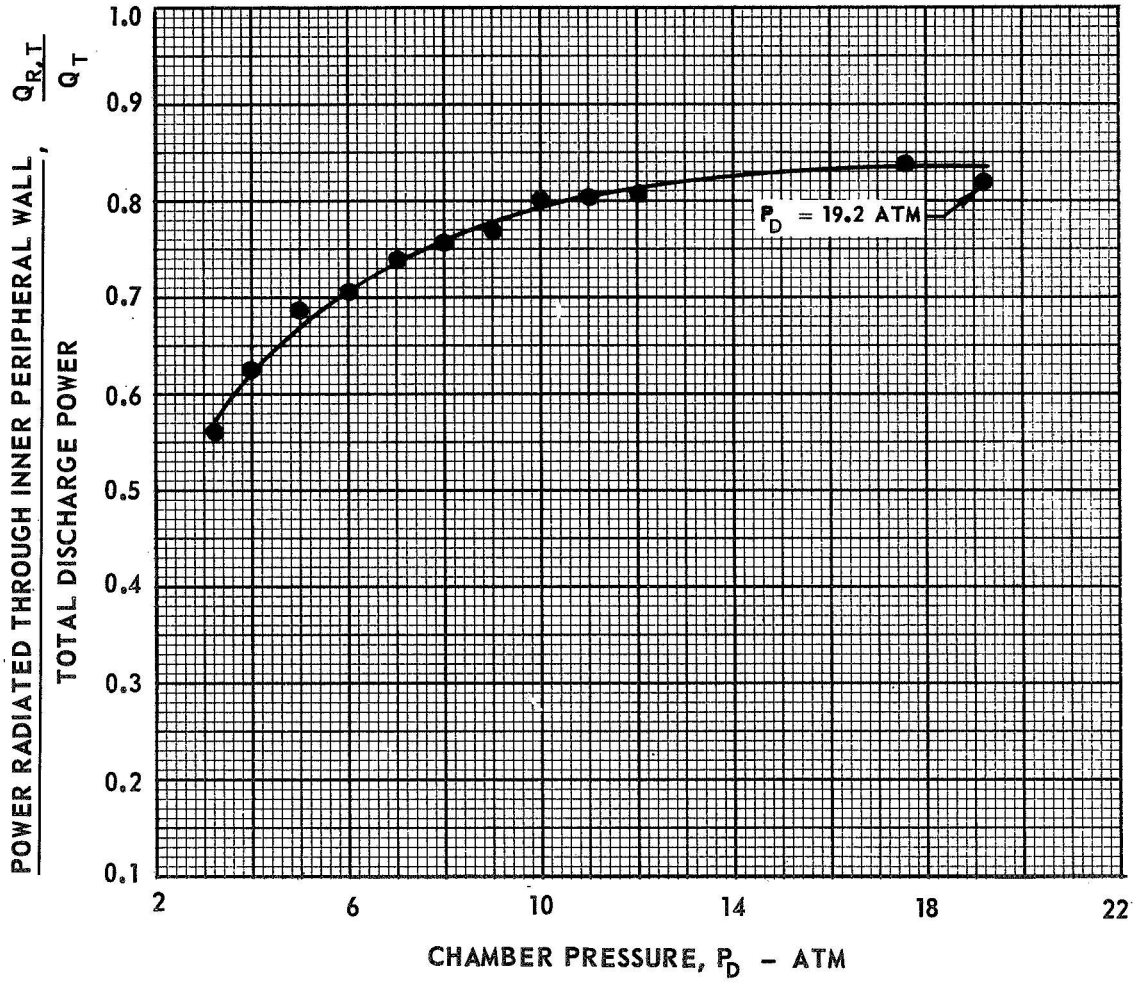

TYPICAL RADIAL DISTRIBUTIONS OF TEMPERATURE OBTAINED IN ARGON R-F PLASMA RADIANT ENERGY SOURCE TESTS

1.2 – MEGW R-F INDUCTION HEATER
SEE FIG. 8(a) FOR SKETCH OF CONFIGURATION USED
SEE REF. 15 FOR SCHEMATIC OF OPTICAL SYSTEM USED
TEMPERATURE PROFILES DETERMINED FROM ARGON CONTINUUM AT 4320Å

CASE I —————— P_D = 1 ATM Q_T = 25 KW
CASE II — — — — P_D = 2 ATM, Q_T = 60 KW
CASE III — — — — P_D = 4 ATM, Q_T = 80 KW
CASE IV ---------- P_D = 5 ATM Q_T = 80 KW
CASE V —— — —— P_D = 6 ATM, Q_T = 120 KW
CASE VI ——·——· P_D = 8 ATM, Q_T = 120 KW

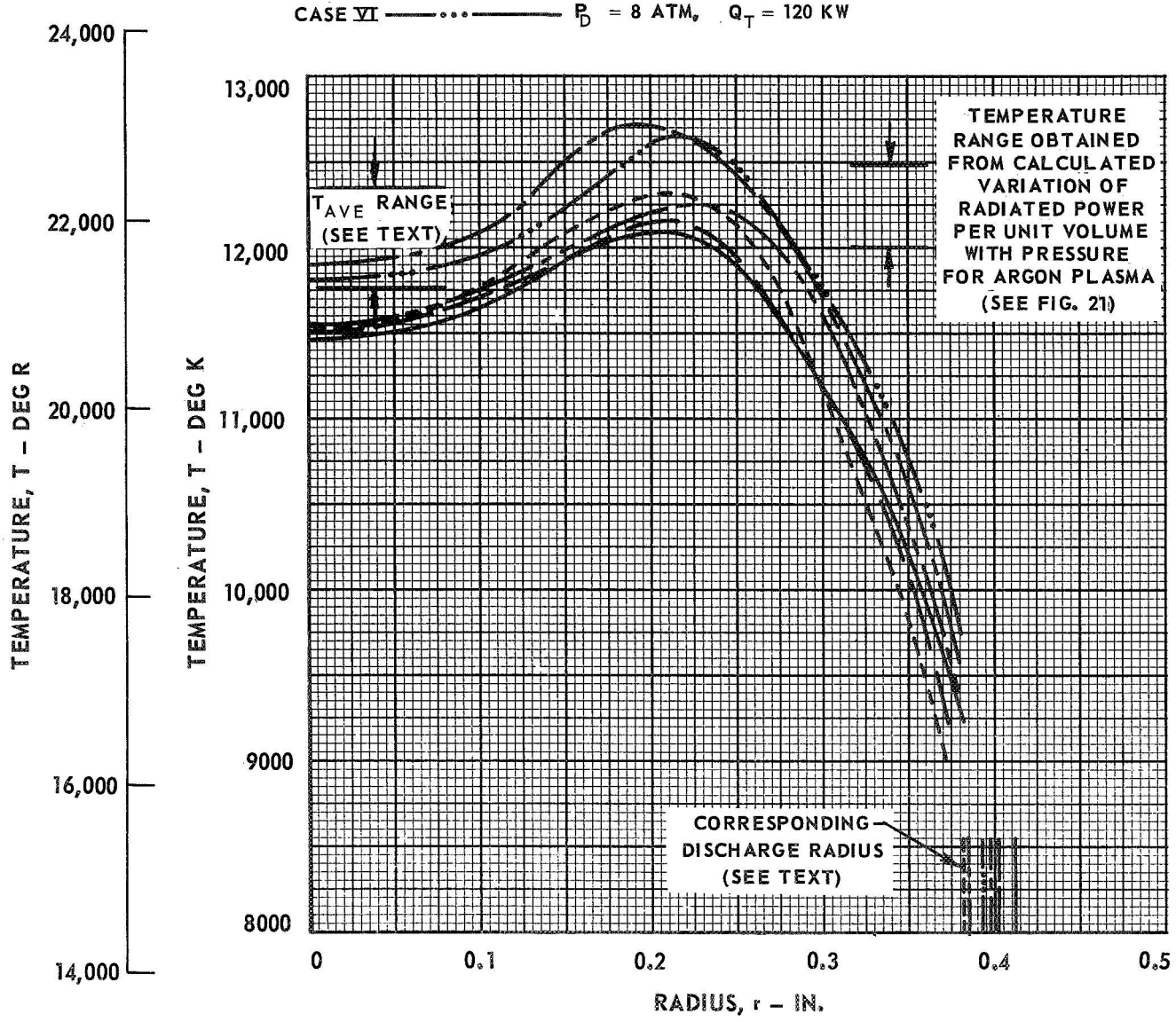

J-910900-4

FIG. 21

COMPARISON OF EXPERIMENTAL AND CALCULATED VARIATION OF RADIATED POWER PER UNIT VOLUME WITH TEMPERATURE FOR AN ARGON PLASMA

CALCULATIONS OBTAINED USING PROCEDURE OF REF. 21 FOR $\lambda = 0.3-1.0$ MICRONS

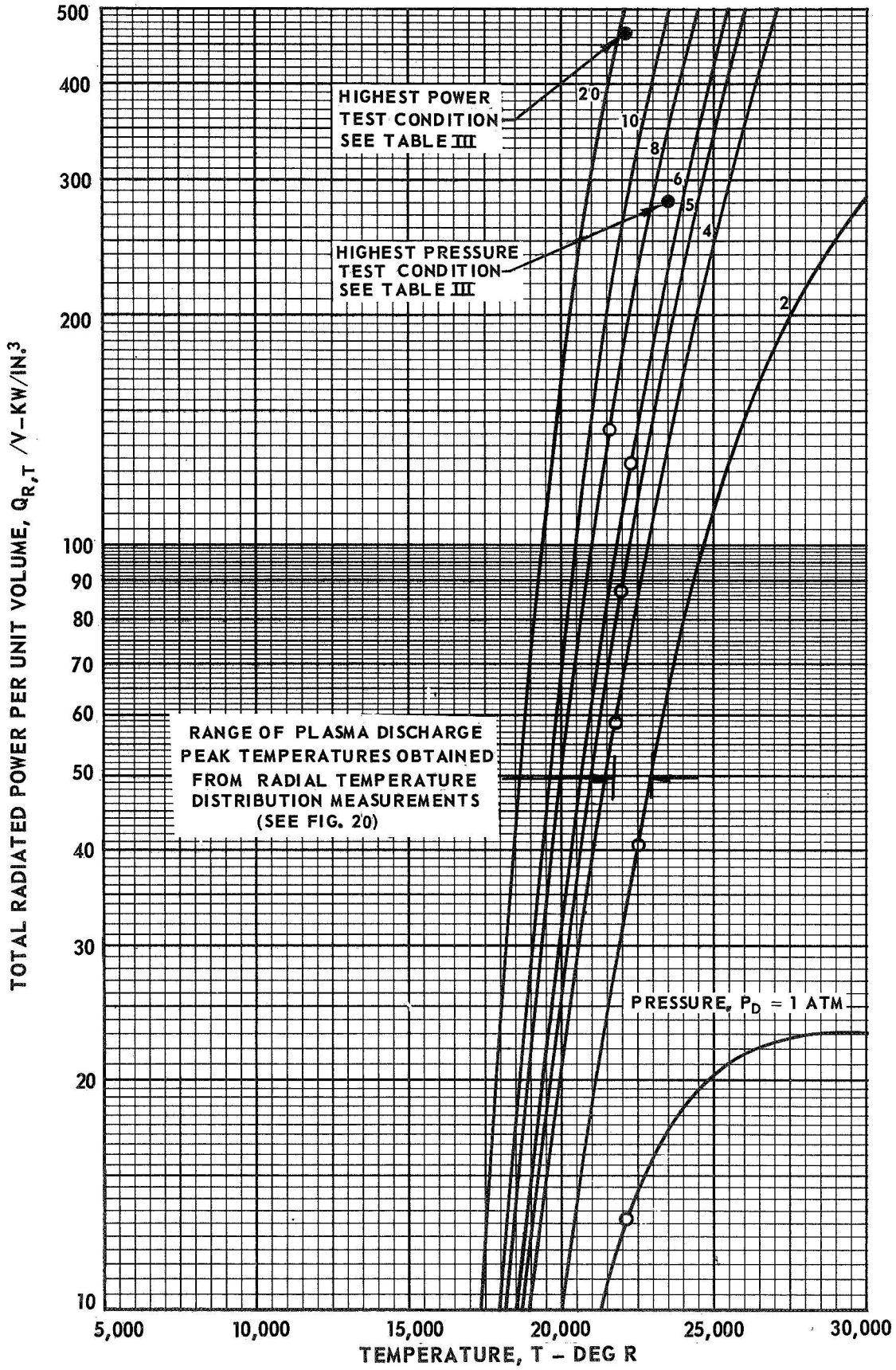

SPECTRAL DISTRIBUTION OF POWER RADIATED THROUGH PERIPHERAL WALL COOLANT

SEE FIG. 8 (a) FOR DETAILS OF TEST CONFIGURATION
NUMBERS IN TABLE EXPRESSED IN KW
NUMBERS IN PARENTHESES IN TABLE EXPRESSED AS PERCENT OF Q_R

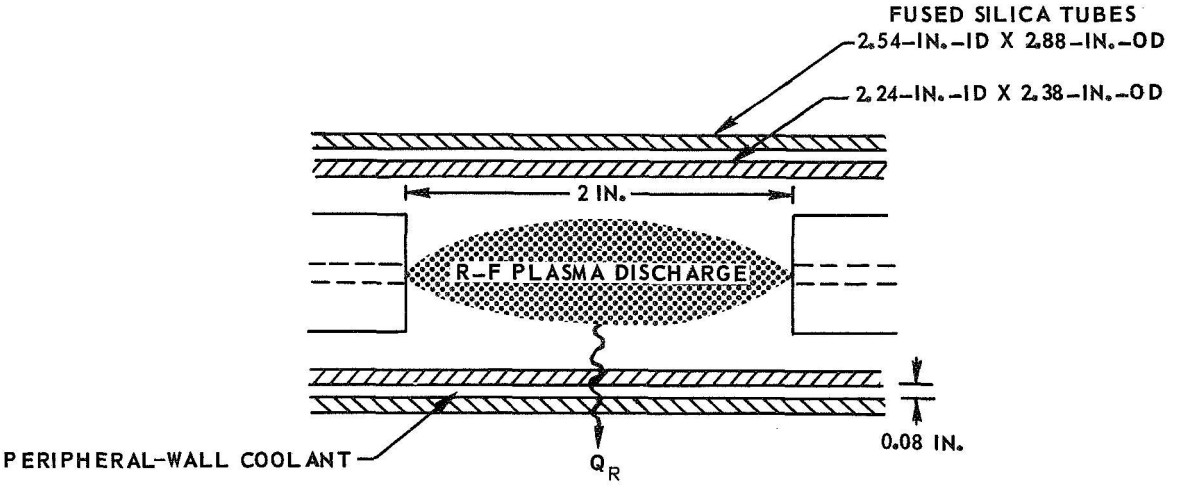

TEST CONDITION	WAVELENGTH BAND - MICRONS			
	0.25-0.30	0.30-0.72	0.72-1.00	1.00-1.30
CASE I Q_T = 55 KW Q_R = 24.5 KW W_A = 0.028 LB/SEC P_D = 3 ATM NO DYE	0.86 (3.5)	5.24 (21.4)	10.4 (42.5)	8.0 (32.6)
CASE II Q_T = 55 KW Q_R = 6.1 KW W_A = 0.028 LB/SEC P_D = 3 ATM 800 PPM NIGROSINE DYE IN ANNULAR COOLING WATER	0.13 (2.1)	0.65 (10.7)	2.9 (47.5)	2.42 (39.7)
CASE III Q_T = 117 KW Q_R = 14 KW W_A = 0.03 LB/SEC P_D = 5 ATM 800 PPM NIGROSINE DYE IN ANNULAR COOLING WATER	0.4 (2.8)	1.56 (11.2)	6.6 (47.1)	5.44 (38.9)

COMPARISON OF EXPERIMENTAL RESULTS FROM 1.2-MEGW R-F RADIANT ENERGY SOURCE WITH RADIATION FLUX LEVELS DESIRED FOR SIMULATION OF THE THERMAL RADIATION FROM A NUCLEAR LIGHT BULB ENGINE AND EARLY IN-REACTOR TESTS

▲ CONFIGURATION HAVING 16 VORTEX INJECTORS AT TWO RADIAL LOCATIONS
SEE FIG. 8 (a) FOR DETAILS OF TEST CONFIGURATION
RANGE OF CHAMBER PRESSURE, P_D = 2 TO 19.2 ATM
RANGE OF ARGON WEIGHT FLOW, W_A = 0.010 TO 0.035 LB/SEC
RANGE OF R-F OPERATING FREQUENCY, f = 5.5629 TO 5.5991 MHz

◢ MAXIMUM RADIATION FLUX LEVEL ACHIEVED IN TEST PROGRAM

——— ——— DESIGN FLUX FOR REFERENCE ENGINE
——— - ——— DESIGN FLUX FOR DERATED ENGINE
- - - - - - - DESIGN FLUX FOR EARLY IN-REACTOR TEST CONFIGURATION (REF. 12)

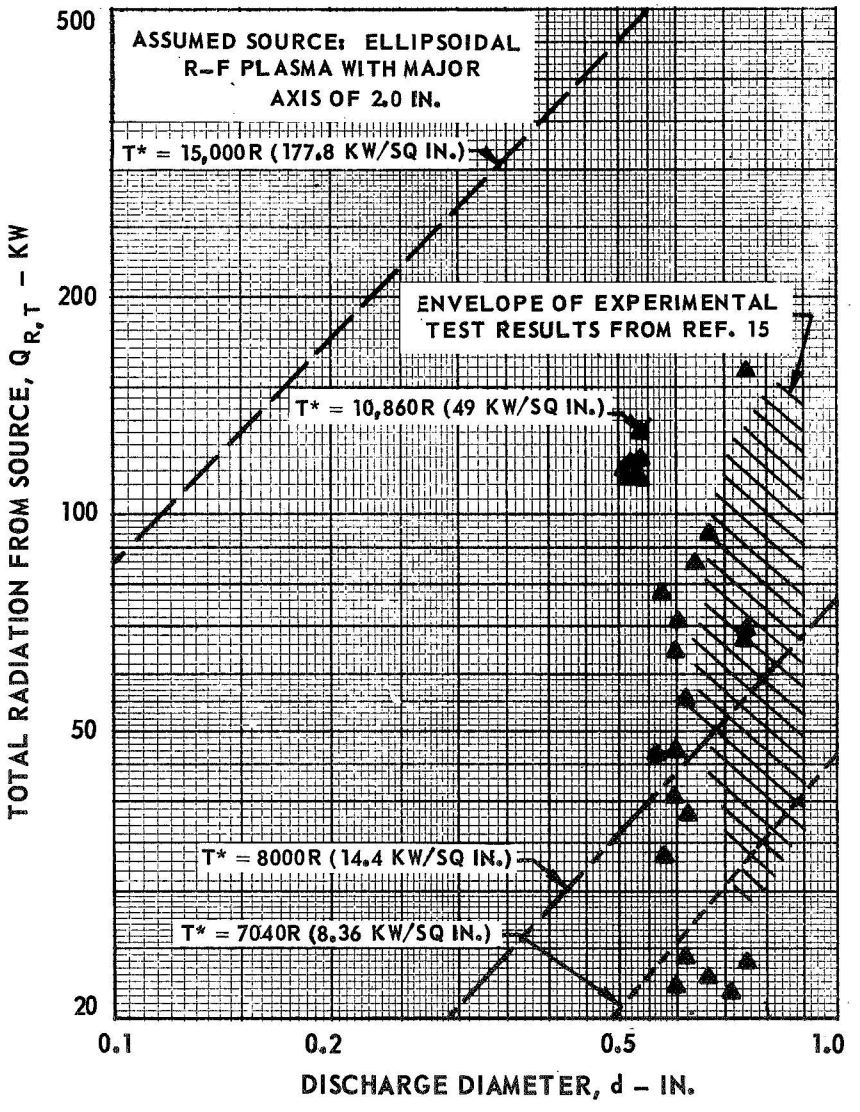

RESULTS OF RESEARCH ON FILAMENT – WOUND PRESSURE VESSELS

(a) SKETCH OF CROSS–SECTION OF FILAMENT–WOUND TUBE INSTALLED IN 80–KW R–F INDUCTION HEATER

SEE REF. 10 FOR DETAILED DISCUSSION OF 80–KW R–F INDUCTION HEATER

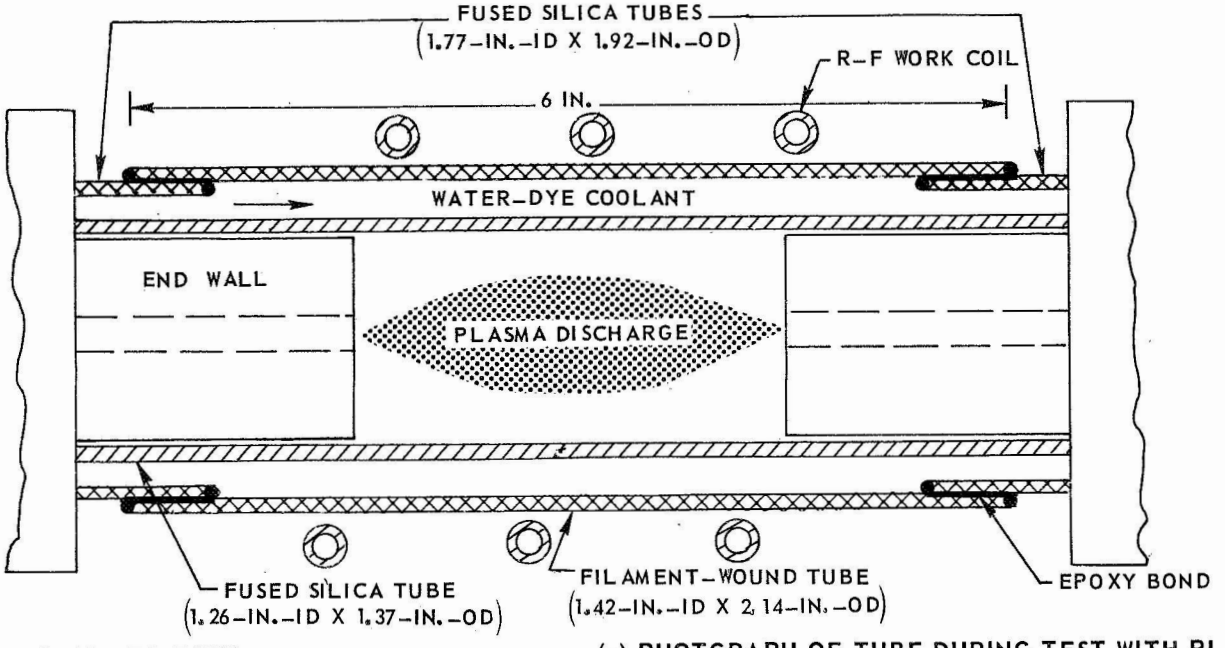

(b) PHOTOGRAPH OF TUBE PRIOR TO TEST

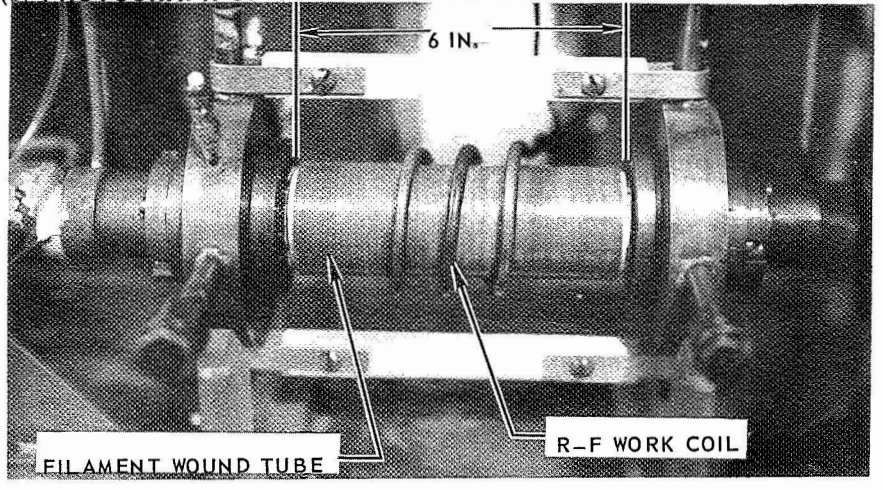

(c) PHOTGRAPH OF TUBE DURING TEST WITH PLASMA

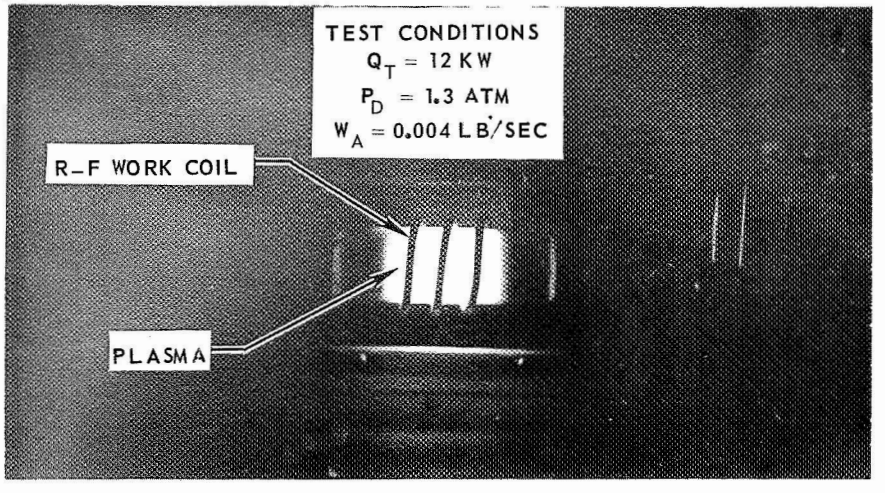

FIG. 24

SCHEMATIC OF OPTICAL SYSTEM FOR DIRECT-ON SPECTRAL MEASUREMENTS OF ARGON PLASMA IN 1.2-MEGW R-F INDUCTION HEATER

(NOT TO SCALE)

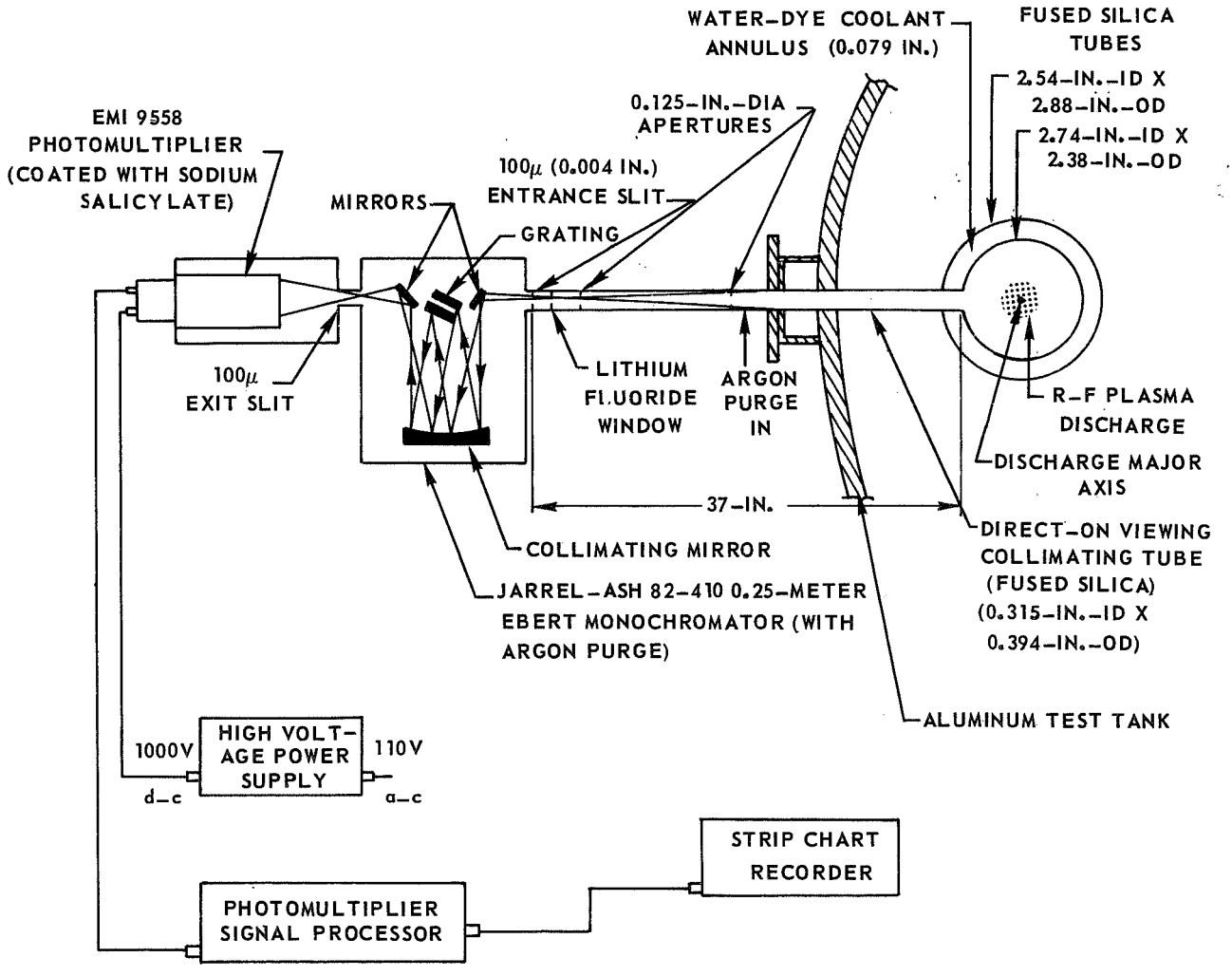

RELATIVE INTENSITY DISTRIBUTIONS OBTAINED FROM DIRECT-ON SPECTRAL MEASUREMENTS OF R-F ARGON PLASMA AND TABLE OF TEST CONDITIONS

CASE	Q_T (KW)	P_D (ATM)	W_A (LB/SEC)	d (IN.)	f (MHz)
I ———	15	1	0.012	0.78	5.5870
II — — —	25	3	0.015	0.75	5.5870
III - - - - - -	75	5	0.024	0.84	5.5870
IV ——— - - ———	98	6	0.031	0.81	5.5870

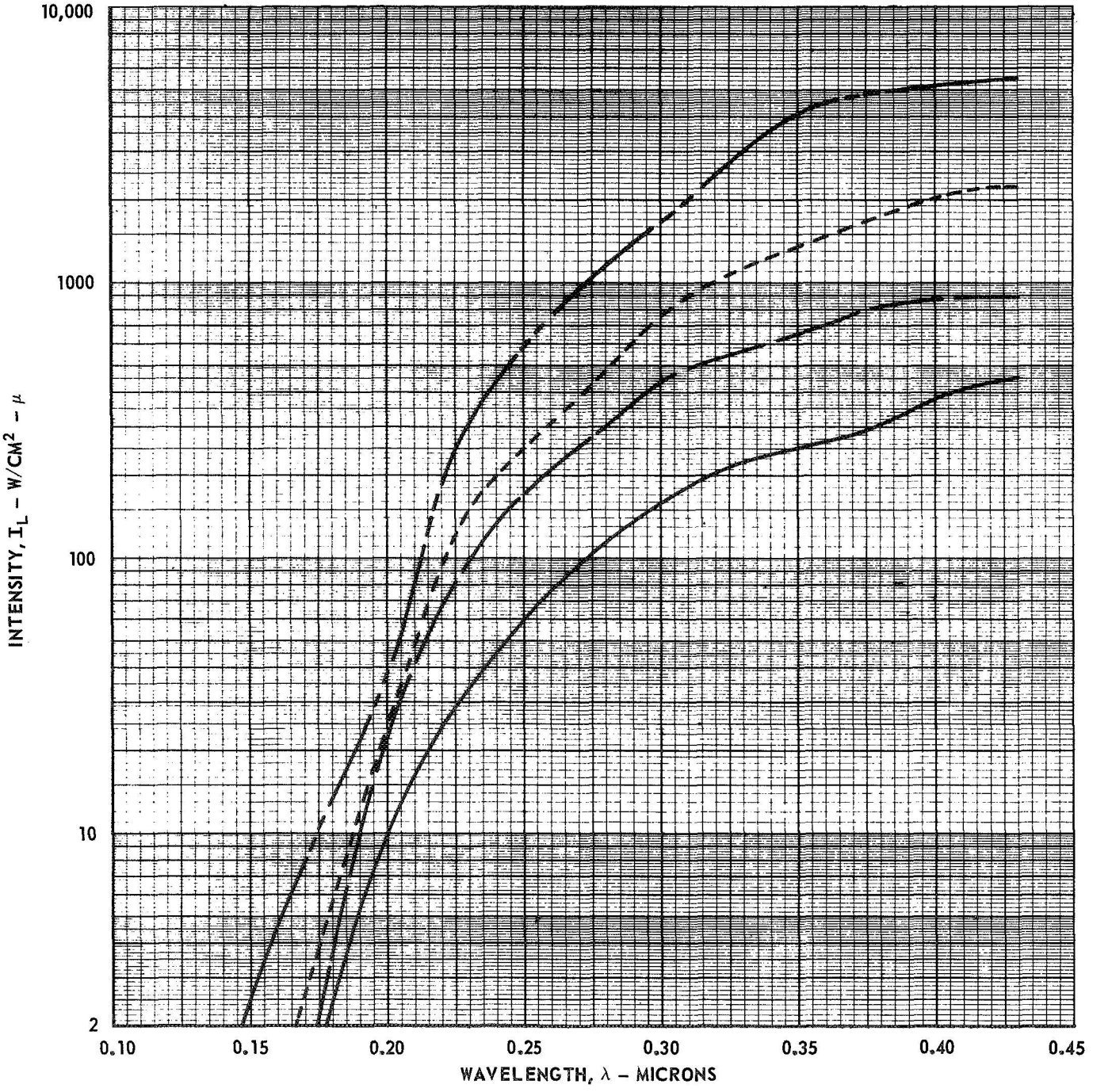

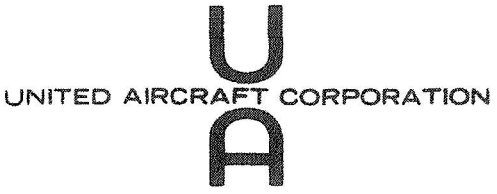
UNITED AIRCRAFT CORPORATION